

## RESEARCH ARTICLE

# Characterizing the Madden–Julian Oscillation in the western Pacific Ocean from a regional coupled ocean–atmosphere model simulation

Vasubandhu Misra<sup>1,2,3</sup>  | C. B. Jayasankar<sup>2,3</sup> 

<sup>1</sup>Department of Earth, Ocean and Atmospheric Science, Florida State University, Tallahassee, Florida, USA

<sup>2</sup>Center for Ocean–Atmospheric Prediction Studies, Florida State University, Tallahassee, Florida, USA

<sup>3</sup>Florida Climate Institute, Florida State University, Tallahassee, Florida, USA

**Correspondence**

Vasubandhu Misra, Department of Earth, Ocean and Atmospheric Science, Florida State University, 1011 Academic Way, Tallahassee, FL 32304, USA.  
Email: [vmisra@fsu.edu](mailto:vmisra@fsu.edu)

**Funding information**

NASA Earth Science, Grant/Award Numbers: 80NSSC19K1199, 80NSSC22K0595

**Abstract**

This study reports on the analysis of the results from a 20 km grid spacing, Regional Coupled ocean–atmosphere Model (RCM) integration over the Western Pacific Warm Pool (WP2). The RCM was integrated over a 20-year period (1986–2005) using reanalysis boundary conditions for the atmosphere and the ocean. This is a first-of-a-kind study with an RCM at 20 km over the WP2. The RCM simulation shows reasonable fidelity of the mean state and of the Madden–Julian Oscillation (MJO). We utilize this successful integration of the RCM to understand a well-known observed feature of MJOs in the WP2 to be of the strongest amplitude during the December–March period of the year. Our analysis of the model integration reveals that the recharge of moist static energy (MSE) prior to peak MJO convection and its discharge during and after the convection explains the MJO in the simulation. The recharge/discharge of the MSE is shown to be largely dictated by horizontal advection, which is stemmed to a small extent by column-integrated radiative heating and surface evaporation. This balance of forces in the evolution of the MSE anomalies and their corresponding variations with sea-surface temperature (SST) anomalies at MJO time-scales in the WP2 is strongest in the December–March period in the RCM simulation.

**KEYWORDS**

analysis, atmosphere, climate, rainfall, regional and mesoscale modelling, tropics

## 1 | INTRODUCTION

The Western Pacific Warm Pool (WP2) assumes significance in the general circulation of the atmosphere, given that it is the host of the ascending branch of the Walker Circulation. Therefore, any variations of the WP2 can potentially result in significant changes in local and remote climate and weather. The spatial extent of the WP2 is relatively large ( $30 \times 10^6 \text{ km}^2$ ), which is, to give a perspective, nearly four times the size of Australia ( $7.69 \times 10^6 \text{ km}^2$ ). The size of WP2 displays considerable variability across

temporal scales (Wyrтки, 1985; Yan *et al.*, 1992; Meinen and McPhaden, 2000; Kidwell *et al.*, 2017). Many studies have clearly established that El Niño/Southern Oscillation (ENSO) is the dominant mode of interannual variability which is characterized by large changes to the size and volume of WP2 (Fu *et al.*, 1986; Webster and Lukas, 1992; Yan *et al.*, 1992; Ho *et al.*, 1995; Meinen and McPhaden, 2000; Kidwell *et al.*, 2017). The Tropical Ocean–Global Atmosphere Coupled Ocean–Atmosphere Response Experiment (TOGA COARE) analyses revealed that WP2 is characterized by variability of precipitation and cloud, forced

largely by the Madden–Julian Oscillation (MJO: Johnson, 1995; Zhang, 2005). In fact, Wang and Xie (1998) argue that the warm pool regime of the WP2, with its moderate mean surface westerlies and the deep thermocline is conducive to coupled ocean–atmosphere unstable modes at intraseasonal time-scales. The MJO influence manifests in a spatial phase relationship between ocean and atmosphere anomalies. For example, many studies indicate that SST anomalies lead the convective anomalies in WP2 by a quarter of a cycle (Kawamura, 1988; Nakazawa, 1995; Zhang, 1996). Similarly, other studies indicate that surface heat flux variations are driving the SST variations in WP2 on the MJO time-scale, with the former leading the latter by a quarter of a cycle (Shinoda *et al.*, 1998; Kemball-Cook and Wang, 2001).

The more recent Cooperative Indian Ocean Experiment on Intraseasonal Variability (CINDY)/Dynamics of the MJO (DYNAMO) field experiment over the equatorial Indian Ocean has revealed a more complex understanding of the air–sea interaction with the passage of MJO (Fu *et al.*, 2015; Moum *et al.*, 2016). For example, Fu *et al.* (2015) find that the SST feedback to MJO is case dependent, with some MJO events exhibiting robust SST anomalies while in other MJO events, the SST anomalies are not as significant. In contrast, Moum *et al.* (2016) report a more robust relationship between SST and MJO over the equatorial Indian Ocean. Using observations collected during DYNAMO, Moum *et al.* (2016) find that the upper ocean introduces a memory effect into the MJO, whereby each successive MJO pulse event is modulated in part by the preceding event. They find that the thermal mixing in the upper ocean from a particular pulse of the MJO might affect the amplitude of the following pulse. These dichotomous conclusions also extend to theories of MJO with one emphasizing the dominance of atmospheric internal dynamics (e.g. Roundy, 2012; Sobel and Maloney, 2013) and the other illustrating the dominant role of air–sea coupling (e.g. Lau and Shen, 1988; Wang and Xie, 1998). But the modelling studies have amplified the contrast of the MJO mechanisms the most. There are several modelling studies that suggest that air–sea coupling significantly improves the various aspects of the MJO observed features (e.g. its organization, strength, propagation, and quadrature in the precipitation–SST relationship: Krishnamurti *et al.*, 1992; Woolnough *et al.*, 2000; Pegion and Kirtman, 2008). Alternatively, global cloud-resolving models that are uncoupled to the ocean model also produce MJO with high fidelity (Miura *et al.*, 2007; Khairoutdinov *et al.*, 2008; Wang *et al.*, 2015). Fu *et al.* (2015) suggest that air–sea coupling plays an important role in the predictability of some MJO events while for others it is strongly controlled by the internal dynamics of the atmosphere. Recent studies point to the importance of the mean state in

the propagation of the MJO, which follows from the moisture mode theory proposed to explain MJO (Raymond and Fuchs, 2009; Sobel and Maloney, 2012, 2013; Adames and Kim, 2016; Wang and Sobel, 2022). These studies suggest that the horizontal advection of the mean moisture by the MJO circulation anomalies plays a significant role in the propagation of the MJO. In fact, Wang and Sobel (2022) suggest that the background zonal moisture gradient is critical for the eastward propagation of the MJO in the tropical Indian and western Pacific Oceans.

In this article, we describe the features of the MJO over the WP2 from a regional coupled ocean–atmosphere model simulation after its validation with observations. This is a first-of-its-kind study where a regional coupled ocean–atmosphere model is used to study WP2 and its variability at intraseasonal scales. The regional coupled ocean–atmosphere simulation of this study reveals some observed features of the MJO on the WP2, which is further analysed to understand MJO. The consistency in the evolution of the state variables of the atmosphere and the ocean and thereby in the ocean–atmosphere fluxes in the regional coupled ocean–atmosphere model simulation of this study lends itself attractively to conducting a detailed investigation to understand MJO over WP2. We analyse the results of our relatively successful model simulation to understand the seasonal preference of the MJO over the WP2 region, and its dependence on the co-evolution of the SST with the overlying atmosphere and contrast them with the recent findings of MJO simulations in global models. Furthermore, Kim *et al.* (2014) also point to several deficiencies in the rendition of MJO in the current and in older versions of the atmospheric reanalysis datasets. In the following section, we describe the model and experiment design, followed by the presentation of results in Section 3 and conclusions in Section 4.

## 2 | MODEL DESCRIPTION AND EXPERIMENT DESIGN

The regional model is the Regional Spectral Model–Regional Ocean Modeling System (RSM–ROMS) with RSM and ROMS being the atmospheric and the oceanic components of the model, respectively. RSM–ROMS has been adopted for many climate studies across tropical and subtropical latitudes (e.g. Li *et al.*, 2014; Misra *et al.*, 2018). The origin of RSM stems from Juang and Kanamitsu (1994) and Juang *et al.* (1997), and that of ROMS is Haidvogel *et al.* (2000) and Shchepetkin and McWilliams (2005). Ever since, both models have undergone changes and the version utilized in this study is described in greater detail in Misra and Jayasankar (2022). In Table S1 we have briefly outlined the physics of RSM and ROMS used in this study.

The simulation is conducted from 1 January 1986 through to 31 December 2005 for a period of 20 years at 20 km grid spacing for both RSM and ROMS. The domain of RSM-ROMS integration is from 29.06°S to 28.59°N, and from 112.1°E to 204.2°E. RSM and ROMS share identical grids. The lateral boundary conditions are from National Centers for Environmental Prediction/Department of the Environment (NCEP-DOE) reanalysis (R2: Kanamitsu *et al.*, 2002) for RSM and Simple Ocean Data Assimilation v2.2.4 (SODA: Carton and Giese, 2008) for ROMS. The lateral boundary conditions for the atmosphere are at 6-hourly intervals while that for the ocean is at monthly intervals. The air-sea coupling interval is 60 min, with the time step for RSM and ROMS at one and 5 min, respectively. The RSM-ROMS simulation is verified with observed rainfall from the National Aeronautics and Space Administration's (NASA's) Integrated Multi-Satellite Retrievals for Global Precipitation Mission version 6 (IMERG) rainfall dataset (Huffman *et al.*, 2019) and SST Optimally Interpolated SST v2 (OISST: Reynolds *et al.*, 2007). Additionally, we also use fifth-generation European Centre for Medium-Range Weather Forecasts (ERA-5) atmospheric reanalysis datasets (Hersbach *et al.*, 2020) to verify upper-air variables. It may be noted that the comparative differences between the model simulation and the corresponding observations are conducted on the observation grid. Since the focus of the study is on MJO we mostly examine the October through to March (ONDJFM) period of the year, which includes the primary peak season of MJO (December–March [DJFM]) in WP2 (Zhang, 2005). However, since we are investigating the seasonal preference of MJO over WP2 we also examine other months of the year in some of our analyses.

To isolate the intraseasonal variability of the MJO, we followed the methodology of a variant of the Multi-dimensional Ensemble Empirical Mode Decomposition following Wu *et al.* (2009). This methodology is described below:

A dataset like  $Y(t, s)$  that varies in space ( $s$ ) and time ( $t$ ) can be decomposed into  $m$  modes of empirical orthogonal functions (EOFs) as:

$$Y(t, s) = \sum_{m=1}^K e_m(s) p_m(t), \quad (1)$$

where  $e_m$  and  $p_m$  are EOFs and principal components (PCs). In the case of precipitation and outgoing long-wave radiation (OLR), we choose to retain the first 50 ( $=K$ ) PCs as the variance explained by successive EOFs began to asymptote (Figure 1). However, precipitation is never a good variable to conduct spatio-temporal analysis given the discontinuous nature of precipitation. Therefore, any analysis technique applied to such variables is likely to

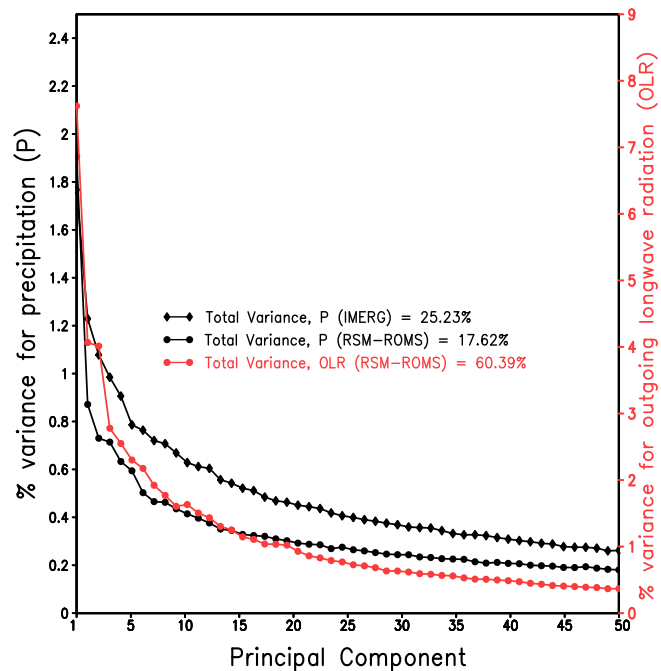


**FIGURE 1** The percentage variance explained by the first 50 principal components of precipitation from regional spectral model-regional ocean modelling system (RSM-ROMS) simulation and IMERG observations, and outgoing long-wave radiation (OLR) from the RSM-ROMS simulation. [Colour figure can be viewed at [wileyonlinelibrary.com](http://wileyonlinelibrary.com)]

produce far less variance than other comparatively continuous variables (e.g. OLR). For instance, the variance explained by the first 50 PCs of OLR is more than three times that of precipitation in the RSM-ROMS simulation (Figure 1). But precipitation is far better observed (spatially and temporally) than most other variables, especially with the advent of IMERG rainfall from NASA's Global Precipitation Measurement mission (GPM: Huffman *et al.*, 2019). Therefore, from a verification standpoint, precipitation is a more attractive variable to describe in a model simulation.

We then conduct an Ensemble Empirical Mode Decomposition (EEMD: Wu and Huang, 2009) on the first 50 PCs. EEMD is a data adaptive signal processing technique, where it decomposes the time series into complete sets of near-orthogonal components called Intrinsic Mode Functions (IMFs). A sample of the two intraseasonal IMFs (5 and 6) for PCs 1, 10, 20, 30, 40 and 50 are shown in Figure S1 for illustration.

We then use these intraseasonal IMFs of the PCs to obtain the intraseasonal anomalies ( $Y'(t, s)$ ) as:

$$Y'(t, s) = \sum_{m=1}^K e_m(s) p_m^f(t), \quad (2)$$

where,  $p_m^f(t) = \text{IMF}_m^5(t) + \text{IMF}_m^6(t)$ .

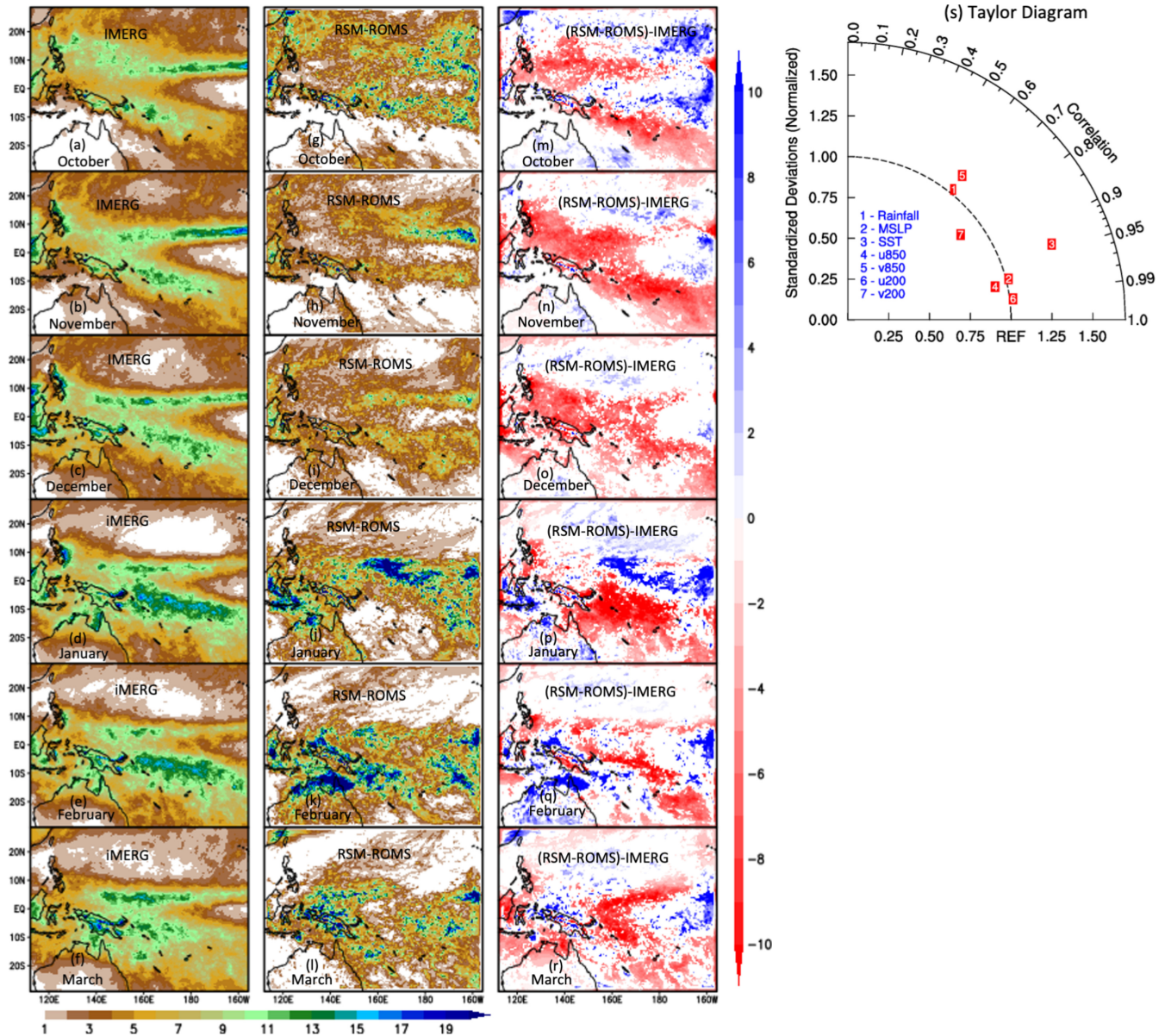


**FIGURE 2** The monthly mean climatological precipitation ( $\text{mm}\cdot\text{day}^{-1}$ ) from (a–f) IMERG, (g–l) regional spectral model-regional ocean modelling system (RSM-ROMS), and (m–r) the corresponding systematic errors of RSM-ROMS (model–IMERG) for (a,g,m) October, (b,h,n) November, (c,i,o) December, (d,j,p) January, (e,k,q) February, (f,l,r) March. Only statistically significant values at 99% two-tailed  $t$ -test are shaded in (m–r). (s) Taylor diagram of the 20-year climatology of October–March mean from RSM-ROMS simulation for precipitation (Rainfall), mean-sea-level pressure (MSLP), SST, zonal wind at 850 hPa (u850) and at 200 hPa (u200), meridional wind at 850 hPa (v850) and at 200 hPa (v200), for the regional domain. Here, IMERG, OISSTv2 and ERA5 are used as the reference dataset for precipitation, SST, the upper-air variables and MSLP, respectively. The values of the pattern correlation coefficient along the arc and the ratio of the standardized variances of the model to observations along the  $x$ - and  $y$ -axes are plotted in the Taylor diagram. [Colour figure can be viewed at [wileyonlinelibrary.com](http://wileyonlinelibrary.com)]

### 3 | RESULTS

#### 3.1 | Monthly climatology

In Figure 2 the monthly mean climatology of rainfall from October through to March is verified. The observations show the gradual evolution of the South

Pacific Convergence Zone (SPCZ) and the corresponding weakening of the intertropical convergence zone (ITCZ) just north of the Equator from October through to February (Figure 2a–e). In March, the SPCZ begins to weaken and the ITCZ begins to strengthen (Figure 2f). The equatorial dry tongue (rainfall  $<1 \text{ mm}\cdot\text{day}^{-1}$ ) is prominent in the October–December period (Figure 2a–c), which

becomes wetter in the subsequent months (Figure 2d–f). The IMERG observations in February (Figure 2e) and March (Figure 2f) suggest the merger of the SPCZ and the ITCZ that pinches off the dry cold tongue region. In the RSM-ROMS simulation, the SPCZ is more zonal and the intensity of both ITCZ and the SPCZ is underestimated (Figure 2g–l and Figure 2m–r). This tendency of a zonal SPCZ is a long-standing issue with global models that continues to persist even now (Bellenger *et al.*, 2014; Grose *et al.*, 2014; Duteil *et al.*, 2019). The dry tongue over the equatorial Pacific Ocean is prevalent from October through to December (Figure 2g–i) in the RSM-ROMS simulation but disappears thereafter (Figure 2j–l) like in observations (Figure 2d–f). However, the pattern correlation coefficient (PCC) of rainfall between RSM-ROMS and IMERG rainfall during ONDJFM is reasonably high (0.66 in Figure 2s). Similarly, the spatial variability of rainfall in RSM-ROMS (represented by the ratio of standard deviation between that of the model to observation) suggests it is comparable to IMERG (Figure 2s). These quantitative measures of the fidelity of the mean precipitation of RSM-ROMS is complimentary to the systematic bias exhibited in Figure 2m–r. Despite the relatively large dry bias over the SPCZ (Figure 2m–r) the comparably high PCC and the comparable variance of the mean precipitation between RSM-ROMS and IMERG, reflect that the large-scale pattern of precipitation and its spatial gradients are well captured in the domain. Other upper-air variables such as zonal wind at 850, 200 hPa, and MSLP also show similar spatial variability as ERA5 with PCC above 0.98 (Figure 2s). The meridional winds at 850 and 200 hPa display slightly lower spatial correlations of 0.65 and 0.83 and normalized standard deviations of 1.1 and 0.85, respectively (Figure 2s).

In Figure 3, the warm bias of the RSM-ROMS over WP2 is most evident. But the observed monthly evolution of the WP2 with the warmest SST shifting from the north to the south of the Equator from October to March (Figure 3a–f) is reasonably well captured in RSM-ROMS (Figure 3g–l). Furthermore, the structure of the WP2 with its horseshoe shape is evident in October and November and its disappearance later in the season is also represented in the RSM-ROMS simulation (Figure 3g–i). The warm bias in the simulation is most extensive and largest in October (Figure 3m) and is least in December (Figure 3o). This pattern of SST bias (Figure 3m–r) is quite consistent with the dry bias of rainfall in Figure 2m–r, which suggests the potential feedback between the two. The dry bias leads to clearer skies, weaker winds, higher downwelling short-wave flux, less mixing, and higher stratification in the upper ocean (not shown) that feed into warming the SSTs further, although the chain of events is not related as linearly as described. However, the spatial

root-mean-square error between the observed SST and RSM-ROMS is comparably small at 0.63°C. The PCC of SST is 0.95 and the normalized standard deviation is 1.33, which yet again suggests that the RSM-ROMS simulation can pick the large-scale structure and spatial variability of SST reasonably well despite the warm bias.

### 3.2 | Features of MJO in RSM-ROMS

The climatological monthly variance of precipitation at the MJO time-scales (20–90 days) for the six months October through to March from IMERG and RSM-ROMS are shown in Figure 4. The seasonal cycle of the intraseasonal time-scale in IMERG is clearly apparent in Figure 4a with the intraseasonal variance growing from October in the SPCZ region before it begins to diminish in March (Figure 4a). The RSM-ROMS simulation at least qualitatively shows a similar seasonal cycle, albeit with weaker variance (Figure 4b). Furthermore, the intraseasonal variability is significantly underestimated in the simulation around the equatorial region and north of it. The corresponding monthly intraseasonal variance of OLR from the RSM-ROMS simulation also shows a similar seasonal cycle feature (Figure S2) with the exception that the arid region of Australia also exhibits large variance in intraseasonal OLR, driven likely by variations in precipitable water (not shown).

The corresponding climatological monthly intraseasonal variance of SST from the RSM-ROMS simulation is shown in Figure 5. The SST intraseasonal variance also shows a similar feature as precipitation and OLR with maximum variance in the months of December, January and February in the SPCZ region. However, note that the region of maximum intraseasonal variance of SST from the RSM-ROMS simulation (Figure 5) does not coincide with the region of maximum intraseasonal variance of either precipitation (Figure 4b) or OLR (Figure S2). In fact, the intraseasonal variance of precipitation in Figure 4b is equatorward to the maximum SST variance in Figure 5. This is understandable given that the intraseasonal variance of precipitation aligns with warmer absolute values of SSTs in the simulation. Several studies have suggested the role of the intraseasonal SST anomalies in preconditioning the environment from increased fluxes and moistening the lower troposphere prior to peak convection (Sobel and Gildor, 2003; Stephens *et al.*, 2004; DeMott *et al.*, 2016). The SST anomalies at the MJO time-scale in the WP2 region are of the order of 0.1°C in the simulation in the months of December, January, February and March (Figure 5).

To examine the propagation features of MJO we regressed the intraseasonal anomalies of precipitation on the corresponding area-averaged anomalies over

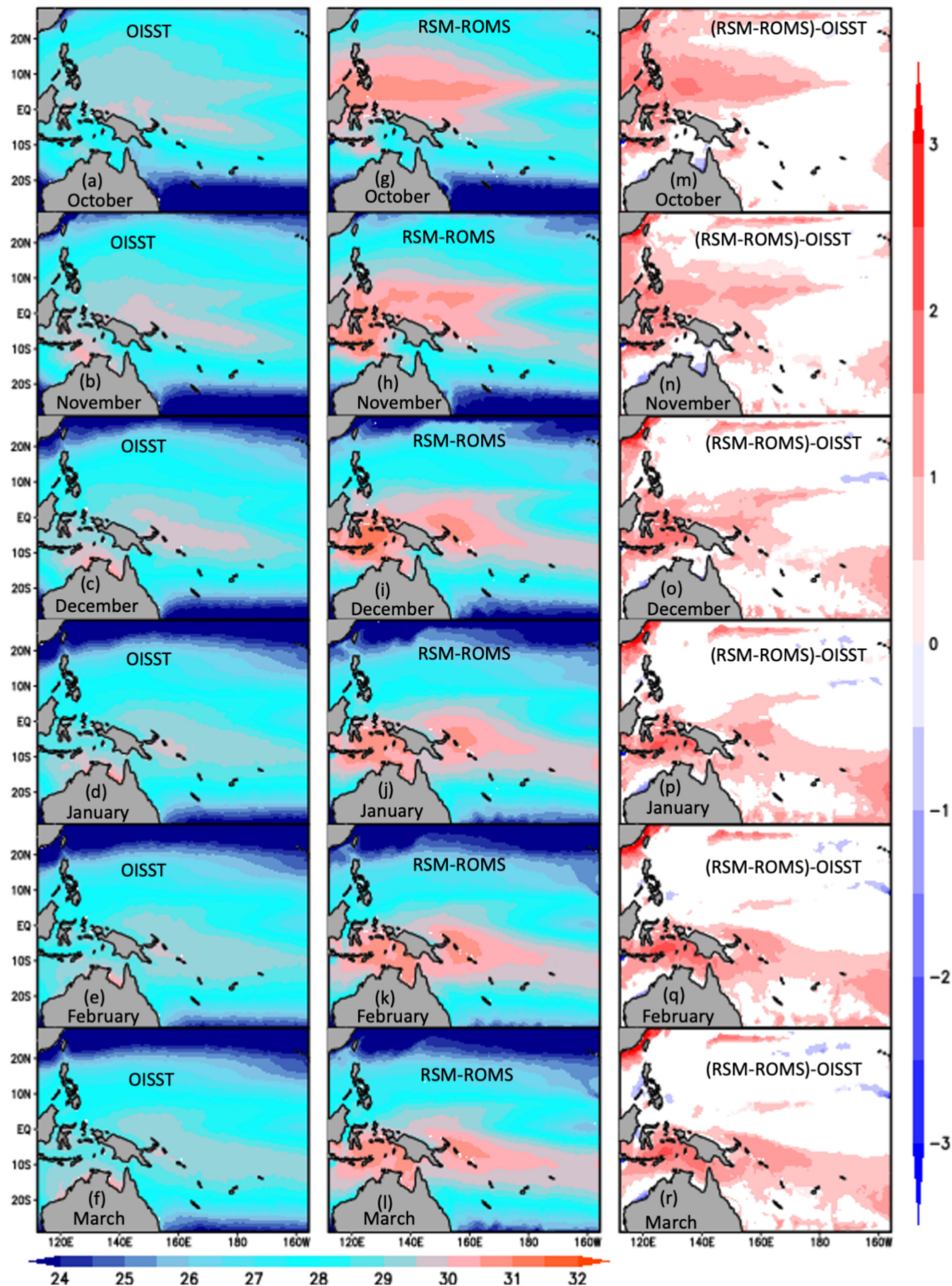


**FIGURE 3** The monthly mean climatological SST ( $^{\circ}\text{C}$ ) from (a–f) OISSTv2, (g–l) regional spectral model–regional ocean modelling system (RSM-ROMS), and (m–r) the corresponding systematic errors of RSM-ROMS (model–OISSTv2) for (a,g,m) October, (b,h,n) November, (c,i,o) December, (d,j,p) January, (e,k,q) February, (f,l,r) March. Only statistically significant values at 99% two-tailed  $t$ -test are shaded in (m–r). [Colour figure can be viewed at [wileyonlinelibrary.com](http://wileyonlinelibrary.com)]

140 $^{\circ}\text{E}$ –160 $^{\circ}\text{E}$  and 15 $^{\circ}\text{S}$ –5 $^{\circ}\text{S}$  (from here on referred to as WP2 and outlined in the first panels of Figures 4a,b and 5) at different lead/lags between  $-30$  and  $+30$  days (Figure 6).

The domain of WP2 was so chosen because the longitude span of WP2 coincides with earlier observational studies on WP2, which was dictated by their use of the data

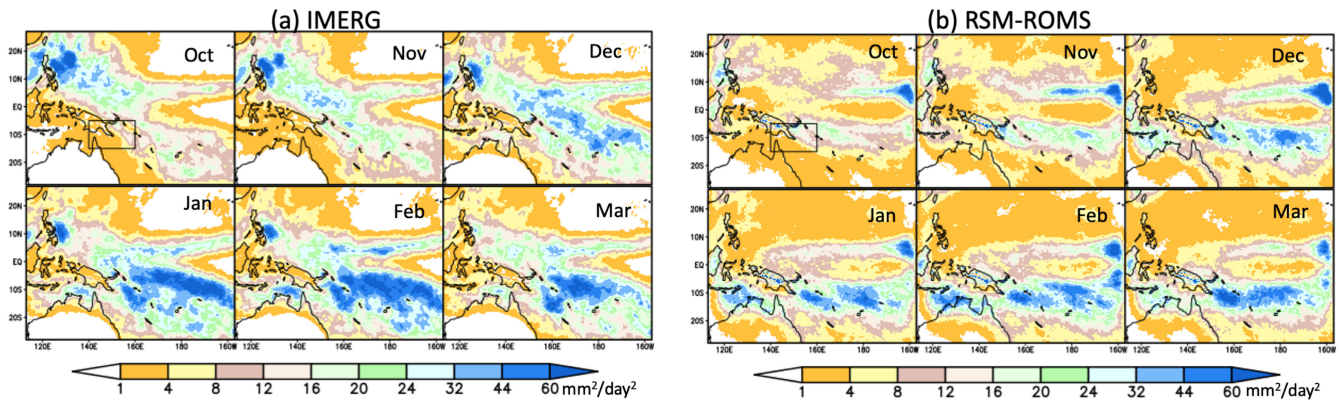
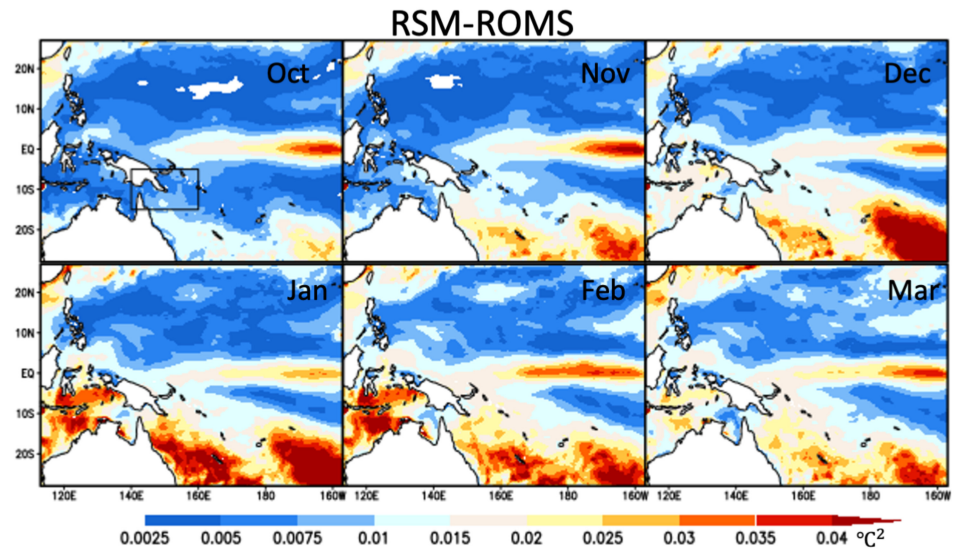


**FIGURE 4** The climatological monthly mean intraseasonal (20–90 days) variance of precipitation anomalies ( $\text{mm}^2 \cdot \text{day}^{-2}$ ) from (a) IMERG and (b) regional spectral model-regional ocean modelling system (RSM-ROMS) simulation. The domain of WP2 ( $140^\circ\text{E}$ – $160^\circ\text{E}$  and  $15^\circ\text{S}$ – $5^\circ\text{S}$ ) is outlined in the first panels of (a,b). [Colour figure can be viewed at [wileyonlinelibrary.com](http://wileyonlinelibrary.com)]

**FIGURE 5** The climatological monthly mean intraseasonal (20–90 days) variance of SST anomalies from the regional spectral model-regional ocean modelling system (RSM-ROMS) simulation from the October to March period. The domain of WP2 ( $140^\circ\text{E}$ – $160^\circ\text{E}$  and  $15^\circ\text{S}$ – $5^\circ\text{S}$ ) is outlined in the first panel. [Colour figure can be viewed at [wileyonlinelibrary.com](http://wileyonlinelibrary.com)]



from the TOGA COARE site (e.g. Stephens *et al.*, 2004; Inoue and Back, 2015) and the latitude span partially captures the region with high MJO variance of precipitation in both observations (Figure 4a) and model simulation (Figure 4b). Furthermore, the features of MJO shown later in this article are more robust further east of this chosen domain (not shown). The IMERG observations indicate a gradual eastward propagation of the anomalies through the 60 days (Figure 6a). Similar eastward propagation of the anomalies is observed in the RSM-ROMS simulation (Figure 6b). The amplitudes of the MJO over WP2 diagnosed from RSM-ROMS and IMERG observations are comparable, and are  $2.54 \pm 0.17$  and  $2.49 \pm 0.11 \text{ mm} \cdot \text{day}^{-1}$ , respectively. However, the simulation underestimates the anomalies across the equatorial region relative to IMERG. The comparison with the corresponding propagation of the OLR anomalies in Figure S3a from the RSM-ROMS simulation is strikingly similar, which further confirms the consistency of the MJO-filtered features of precipitation

in the simulation despite the comparatively less variance explained by the isolated PCs as shown in Figure 1.

To further illustrate the zonal propagation, a Hovmöller diagram is constructed in Figure 7, which shows the regression of the intraseasonal anomalies, latitudinally averaged between  $15^\circ\text{S}$  and  $5^\circ\text{S}$  on the corresponding area-averaged anomalies over WP2. In comparing Figure 7a,b, we clearly see the robust and comparable zonal propagation of precipitation both in IMERG and RSM-ROMS simulation, respectively. The RSM-ROMS simulation (Figure 7b) however suggests a slight weakening of the anomalies of precipitation east of  $170^\circ\text{E}$  relative to IMERG (Figure 7a). The phase speeds of MJO determined following Chen and Wang (2018) are  $5.6$  and  $5.4 \text{ m} \cdot \text{s}^{-1}$  in Figure 7a,b, respectively. The similarity of Figure 7b with the corresponding Hovmöller diagram of OLR anomalies from the RSM-ROMS simulation in Figure S3b, further confirms the diagnosis of the zonal propagation of the MJO anomalies of precipitation.

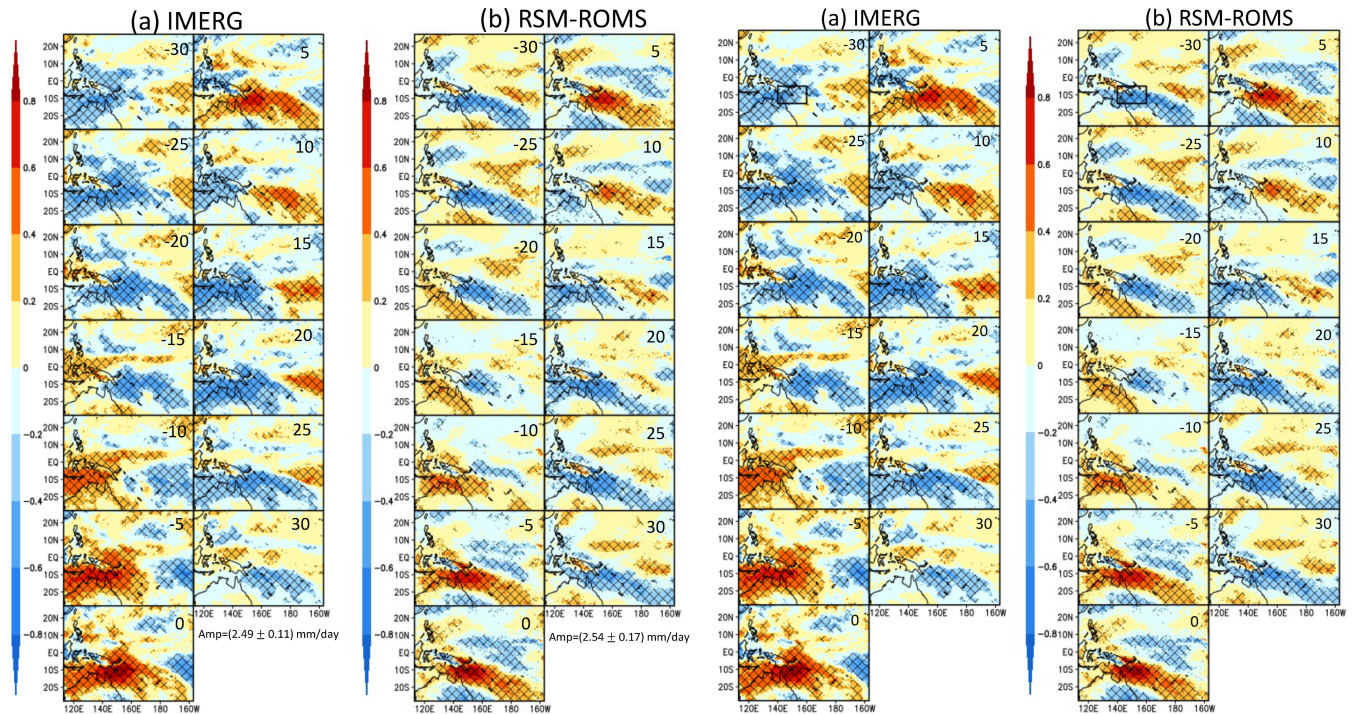


**FIGURE 6** The regression of the intraseasonal (20–90 days) precipitation anomalies on the corresponding area-averaged intraseasonal precipitation anomalies over WP2 (140° E–160° E and 15° S–5° S; outlined in the first panel of Figures 3 and 4) from (a) IMERG and (b) regional spectral model-regional ocean modelling system (RSM-ROMS) simulation. The lead/lag in days is shown in the top-right corner of each panel with negative and positive days suggesting lead and lag with respect to the area-averaged anomalies. The hatched regions show statistically significant regions at 95% confidence interval according to the  $t$ -test. The amplitude (Amp,  $\text{mm}\cdot\text{day}^{-1}$ ) of the intraseasonal anomalies of precipitation with its standard error over WP2 is indicated at the bottom of each panel. [Colour figure can be viewed at [wileyonlinelibrary.com](http://wileyonlinelibrary.com)]

Similarly, Figure 7c shows the zonal propagation of the intraseasonal SST anomalies from the RSM-ROMS simulation with amplitude over WP2 being  $0.1^\circ\text{C}$  and a phase speed of  $2.5\text{ m}\cdot\text{s}^{-1}$ , which shows a comparably weak eastward propagation and a much stronger standing oscillation between the longitudes of  $140^\circ\text{E}$  and  $160^\circ\text{E}$ .

Recently, Kim *et al.* (2019) reported that most operational climate models suffer from grave mean biases in the WP2 region that results in underestimation of MJO amplitude, weak eastward propagation, and struggle to predict the MJO propagation through the Maritime Continent (MC). For example, Kim *et al.* (2019) report that the operational climate models in the Subseasonal Experiment (SubX) and Subseasonal to Seasonal (S2S) repositories fail to predict the propagation of MJO convection beyond 10 days owing to dry bias in the lower troposphere that hinders the horizontal moisture advection east of the MJO convective anomaly. On the other hand, Ahn *et al.* (2020) indicate that CMIP6 models simulate the MJO propagation across the MC more realistically than the CMIP5 models. They find this improvement is a result of improved horizontal moisture advection from the more realistic simulations of the horizontal mean-state moisture gradients around the MC. In light

of these findings, the MJO simulation in RSM-ROMS is relatively encouraging. Additionally, many other studies indicate global models with reasonable MJO simulation have a relatively poorer fidelity of the mean state (Hannah and Maloney, 2011; Chen and Mapes, 2018; Ahn *et al.*, 2019). Therefore, simulating the features of MJO rainfall anomalies amidst a reasonable simulation of the mean state is a stiff challenge for any numerical climate model.

To further illustrate this amplitude modulation of the MJO across seasons, we show in Figure S4 the time evolution of the intraseasonal precipitation anomalies averaged over WP2 for each year from 2001 to 2020 and 1986 to 2005 from IMERG and RSM-ROMS simulation, respectively. It is clear from both the observations and the simulation that December–January–February–March (DJFM) is the peak season for the intraseasonal anomalies in the WP2 region when its amplitude is the largest in the year. Le *et al.* (2021) find from the analysis of the twentieth-century simulations of the CMIP6 models that they seem to reasonably capture the MJO propagation speed but significantly underestimate their amplitude, thereby undermining its contribution to intraseasonal precipitation variability over the Maritime Continent region. There are however

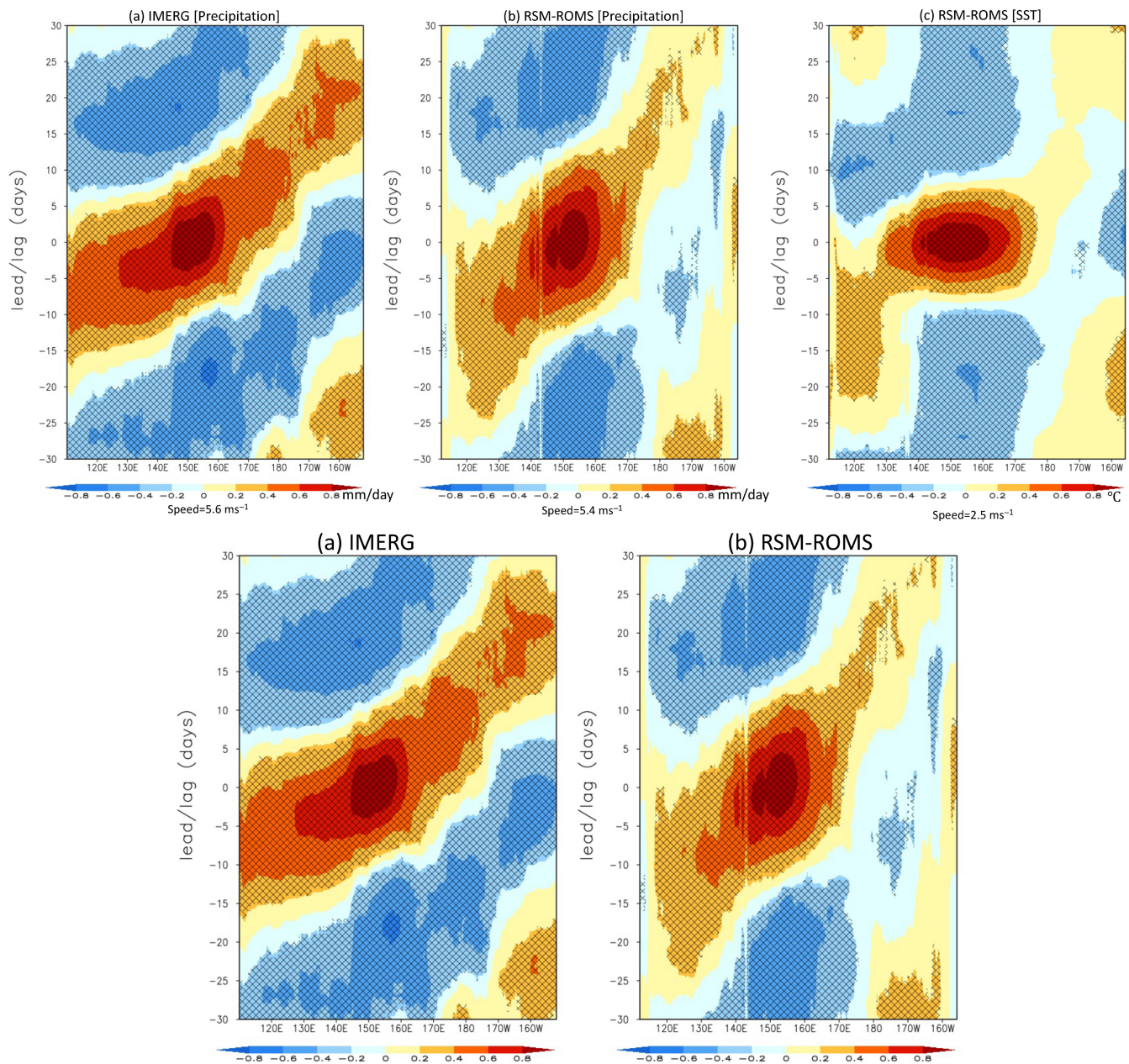


**FIGURE 7** The regression of the intraseasonal (a,b) precipitation ( $\text{mm}\cdot\text{day}^{-1}$ ) and (c) SST anomalies averaged between  $15^{\circ}\text{S}$  and  $5^{\circ}\text{S}$  on the corresponding area-averaged intraseasonal (20–90 days) precipitation anomalies over WP2 ( $140^{\circ}\text{E}$ – $160^{\circ}\text{E}$  and  $15^{\circ}\text{S}$ – $5^{\circ}\text{S}$ ) from (a) IMERG and (b,c) regional spectral model-regional ocean modelling system (RSM-ROMS) simulation. The negative and positive days along the ordinate suggest lead and lag with respect to the area-averaged anomalies. The hatched regions show statistically significant regions at 95% confidence interval according to the  $t$ -test. The phase speed (Speed,  $\text{m}\cdot\text{s}^{-1}$ ) of the intraseasonal anomalies over WP2 are indicated at the bottom of each panel. [Colour figure can be viewed at [wileyonlinelibrary.com](http://wileyonlinelibrary.com)]

some exceptions in the RSM-ROMS simulation with years 1999–2000, 2003–2004 and 2004–2005 when there is a comparably large amplitude anomaly in November. Furthermore, Figure S4 shows both in observations and in the RSM-ROMS simulation that the successive pulses of MJO precipitation anomalies have no apparent relation to each other as noted over the Indian Ocean (Moum *et al.*, 2016). For example, the relatively large or low amplitude MJO in the DJFM season in any given year has no systematic

precedence and succession of low or high amplitude MJO anomalies (Figure S4), respectively.

### 3.3 | Moist static energy and surface fluxes

An emerging consensus on the MJO dynamics is the recharge–discharge theory, in which moist static

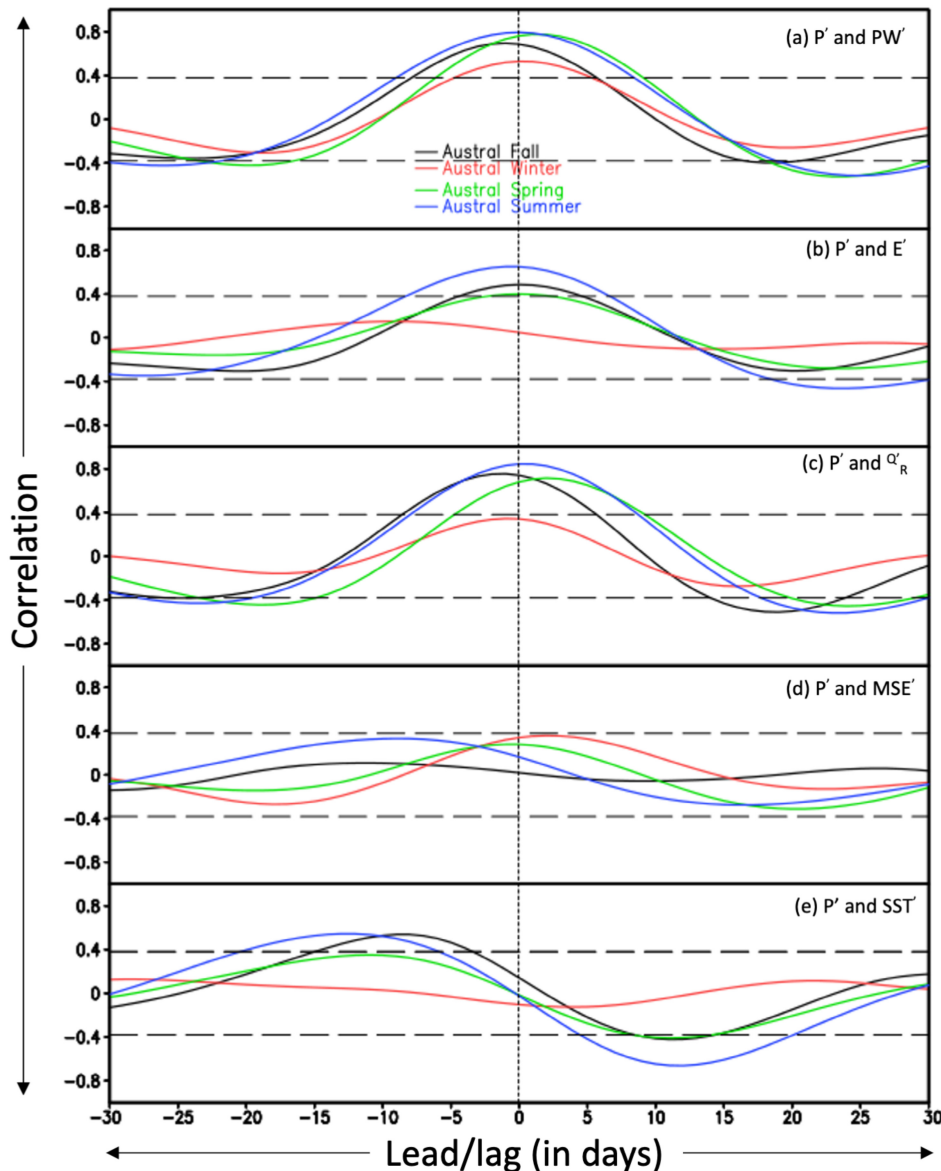


**FIGURE 8** The lead-lag correlation between Madden–Julian Oscillation (MJO) anomalies of (a) precipitation ( $P'$ ) and precipitable water ( $PW'$ ), (b)  $P'$  and surface evaporation ( $E'$ ), (c)  $P'$  and column-integrated radiative heating ( $Q'_R$ ), (d)  $P'$  and  $MSE'$ , and (e)  $P'$  and  $SST'$  from the regional spectral model-regional ocean modelling system (RSM-ROMS) simulation for the four seasons of austral autumn (April–May), austral winter (June–July–August), austral spring (September–October–November), and austral summer (December–January–February–March). The horizontal long dashed lines indicate the 90% confidence interval according to the  $t$ -test. The negative and positive lags indicate the first variable ( $P'$ ) is lagging and leading the second variable indicated in the panel, respectively. [Colour figure can be viewed at [wileyonlinelibrary.com](http://wileyonlinelibrary.com)]

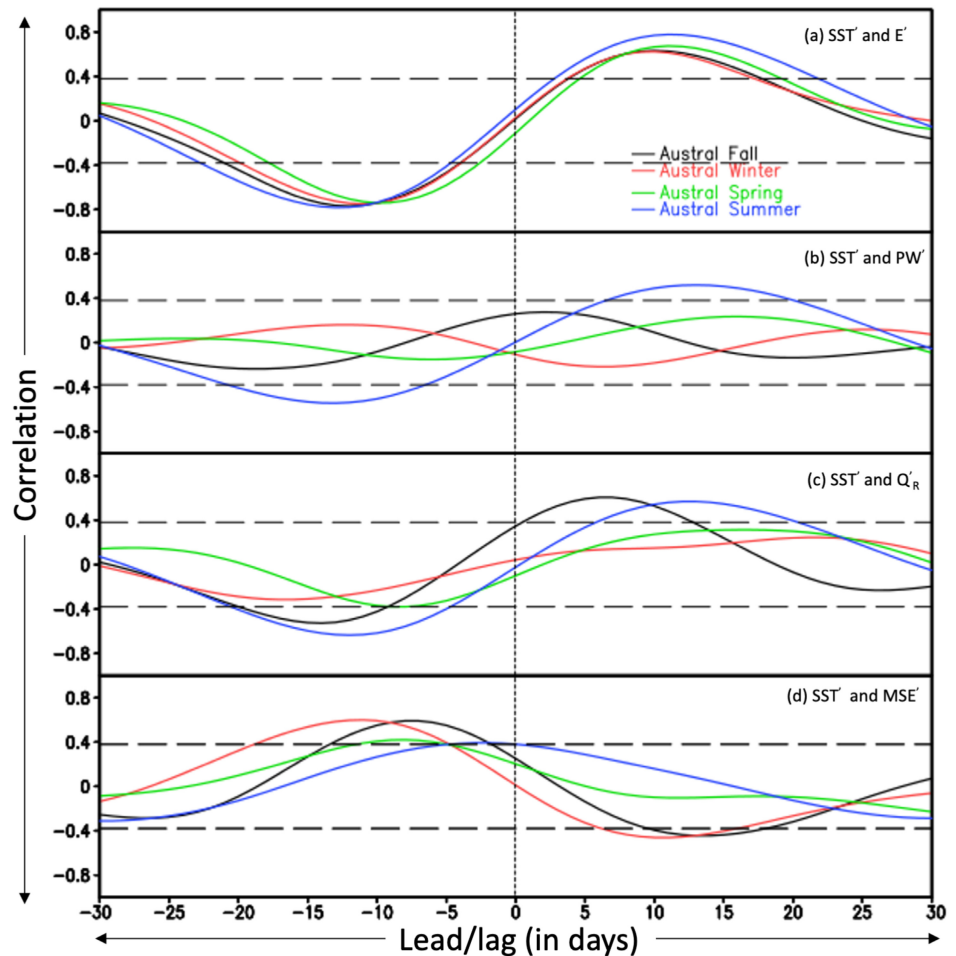
energy (MSE) gradually builds up before the MJO precipitation peaks, which is then subsequently discharged during and after the convection (Hendon and Liebmann, 1990; Bladé and Hartmann, 1993; Maloney and Hartmann, 2001; Sobel and Gildor, 2003; Kiladis *et al.*, 2005). Inoue and Back (2015) using the TOGA-COARE datasets show a recharge–discharge mechanism of MSE in the atmospheric column for the maintenance of the MJO. This mechanism refers to the import of MSE via low-level horizontal advection (which becomes more dominating as time-scales increase from the mesoscale to the intraseasonal scales) that amplifies the convection at MJO time-scales. At shorter time-scales (<10 days), Inoue and Back (2015) show that the vertical advection of MSE is dominating the MSE budget. Furthermore, the variability of the column MSE in the tropics is dictated by the corresponding changes in the precipitable

water, which is tightly coupled to the precipitation anomalies owing to the weak temperature gradient in the tropics (Yasunaga and Mapes, 2012; Sobel *et al.*, 2014).

In Figure 8a–e we show the correlations of filtered MJO precipitation anomalies with corresponding precipitable water, local evaporation, atmospheric radiative heating, MSE, and SST anomalies, respectively, across the four seasons of austral autumn (April–May), austral winter (June–July–August), austral spring (September–October–November), and austral summer (DJFM) from the RSM-ROMS simulation.

The relationship between precipitation and precipitable water is consistent across the seasons with precipitation and precipitable water having the highest positive correlation at zero lag (Figure 8a), which suggests that precipitation and precipitable water anomalies are tightly coupled in the simulation as noted in earlier

**FIGURE 9** The lead–lag correlation between MJO anomalies of (a) SST' and surface evaporation ( $E'$ ), (b) SST' and precipitable water ( $PW'$ ), (c) SST' and column-integrated radiative heating ( $Q'_R$ ), and (d) SST' and MSE' from the RSM-ROMS simulation for the four seasons of austral autumn (April–May), austral winter (June–July–August), austral spring (September–October–November), and austral summer (December–January–February–March). The horizontal long dashed lines indicate the 90% confidence interval according to the  $t$ -test. The negative and positive lags indicate the first variable (SST) is lagging and leading the second variable indicated in the panel, respectively. [Colour figure can be viewed at [wileyonlinelibrary.com](http://wileyonlinelibrary.com)]



observational studies. Similarly, the filtered anomalies of precipitation and local evaporation at MJO time-scales are coupled strongly at zero lag except in the austral winter, when the relationship is insignificant (Figure 8b). The corresponding correlations of precipitation with column-integrated radiative heating in Figure 8c also show they are in phase across seasons at zero lag with slight variations. For example, in the austral winter, the correlations are much weaker than in the rest of the year (Figure 8c).

Figure 8d indicates that the MSE leads precipitation, by about 10 days during the DJFM (austral summer) season while in the austral winter, MSE is lagging precipitation by a few days. In the spring season, they are in phase, and in the autumn the relationship is weak (Figure 8d). The correlations of the precipitation and MSE anomalies in DJFM in Figure 8d are arguably weak and barely reach statistical significance. The lead/lag relationship of precipitation anomalies with SST anomalies in Figure 8e reveals that in the RSM-ROMS simulation, the SST warms 15 days prior to peak convection and then cools in about 12–15 days post-convection, consistent with observations (Stephens *et al.*, 2004).

The lead/lag relationships of SST anomalies at the MJO time-scale over WP2 with corresponding anomalies of

surface evaporation, precipitable water, column-integrated radiative heating, and MSE anomalies from the RSM-ROMS simulation are illustrated in Figure 9a–d, respectively. These figures suggest a robust relationship, wherein surface evaporation (Figure 9a), moistening of the air column (Figure 9b), column-integrated radiative heating (Figure 9c), and MSE (Figure 9d) lead the SST between ~10 and 15 days. In other words, Figure 9 suggests that in the simulation as wind-driven evaporation picks up, SST drops, the air column moistens, radiative heating and MSE builds before peak convection occurs and then the discharge of MSE begins with associated drying of the column, radiative cooling from relatively clear skies, and gradual warming of the SST. It is interesting to note in Figure 9 that the austral summer season shows the strongest relationship of SST anomalies with the anomalies of all the variables in the year except with MSE. Furthermore, the lead between the build-up of MSE and SST anomalies is shortest in the austral summer season (Figure 9d). But it may be noted that the correlations in the DJFM season between MSE and SST anomalies are less robust than in other seasons (Figure 9d).

Inoue and Back (2015) argue that the analysis of the MSE of the atmospheric column will provide a better

understanding of the amplification and decay of convection. To show this, we computed the MSE budget over the region 15°S–5°S and 140°E–160°E from the RSM-ROMS simulation. The MSE budget equation is given as:

$$\frac{\partial \langle \Gamma_m \rangle}{\partial t} = -\nabla \cdot \langle \Gamma_m \mathbf{V} \rangle + EF + Q_R. \quad (3)$$

In Equation (3), the angular brackets represent vertical integration,  $\Gamma_m$  is the MSE,  $\mathbf{V}$  is the three-dimensional winds,  $EF$  is enthalpy (=sensible + latent) or surface heat fluxes, and  $Q_R$  is the column-integrated net radiative heating (obtained as the difference in the radiative flux between the bottom and the top of the atmosphere). For the MJO time-scales, Equation (1) can be filtered at the 20–90 days time-scale ( $'$ ) to rewrite the equation as:

$$\frac{\partial \langle \Gamma_m \rangle'}{\partial t} = -\nabla \cdot \langle \Gamma_m \mathbf{V} \rangle' + EF' + Q_R'. \quad (4)$$

We further area-average the budget terms in Equation (4) over the WP2 region. The divergent flux of the MSE can be further broken down into horizontal and vertical advection terms:

$$\nabla \cdot \langle \Gamma_m \mathbf{V} \rangle' = \langle \Gamma_m \cdot \nabla \mathbf{V}_H \rangle' + \langle \Gamma_m \frac{\partial \omega}{\partial p} \rangle'. \quad (5)$$

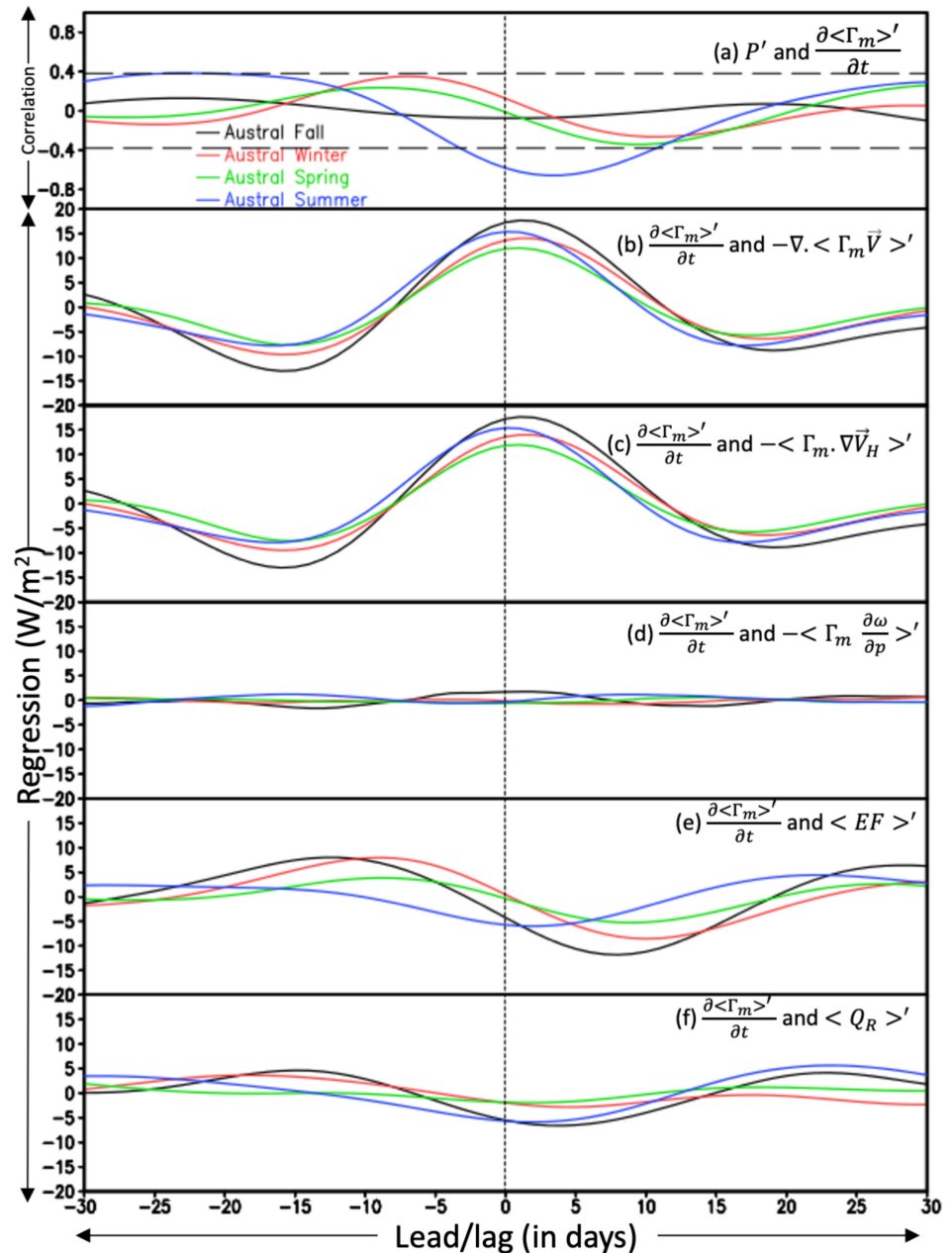
The divergent flux term in Equation (4) is computed as a residual and in Equation (5) the horizontal advection term is computed as a residual of the difference between the divergent flux of MSE and the vertical advection of MSE.

In Figure 10, we show the lead/lag relationship of each of these forcing terms in Equation (4) with the time tendency of the anomalous MSE ( $\frac{\partial \langle \Gamma_m \rangle'}{\partial t}$ ). But to begin with, the lead/lag correlation of precipitation with  $\frac{\partial \langle \Gamma_m \rangle'}{\partial t}$  is shown in Figure 10a. Kiranmayi and Maloney (2011) indicate that in the tropical Indian and western Pacific Ocean, anomalous precipitation and the tendency of MSE are in quadrature, with the peak in tendency field leading the former. Figure 10a shows the austral summer season exception to the quadrature relation with the correlations being strongest between precipitation and the tendency of MSE close to lag zero. Furthermore, Figure 10a suggests the build-up of MSE prior to the precipitation peak (recharge phase) and its attenuation at and after the peak (discharge phase). In the austral winter and spring seasons this relationship exists albeit slightly weaker and at shorter lead/lag times, while the austral autumn season exhibits the weakest relationship. The rest of the panels in Figure 10 show the relationship of the tendency of the anomalous MSE with the rest of the forcing terms in Equations 4 and 5. In Figure 10b–f we prefer to show

the regression of the forcing terms on the tendency of MSE so that the relative magnitude of the forcing terms can be gauged. Figure 10b shows that the tendency of anomalous MSE is dominated by the divergent flux term of MSE and they are in phase. This divergent flux of MSE is further dominated by the horizontal advection of MSE (Figure 10c) and less so by the vertical advection of MSE (Figure 10d) as was noted in other modelling and observational studies (Maloney, 2009; Maloney *et al.*, 2010; Kiranmayi and Maloney, 2011; Inoue and Back, 2015). However, the near lack of relationship with the vertical advection of anomalous MSE is likely a notable bias of the model simulation given their acknowledged importance in other studies (Haertel *et al.*, 2008; Inoue and Back, 2015; Adames and Kim, 2016; Adames and Maloney, 2021). Furthermore, as noted in Maloney (2009), computing the advection terms from model output is different from the way it is done in the model dynamical core which often results in large residuals. Nonetheless, Figure 10c suggests that the recharge and discharge of MSE at pre- and post-MJO convection in the RSM-ROMS is to a large part accounted for by the horizontal advection of MSE, respectively. Furthermore, this is true across all seasons. The lead/lag relationship between the tendency of anomalous MSE and enthalpy fluxes (Figure 10e) shows that the former lags the latter by a few days. Figure 10e suggests that anomalous enthalpy fluxes slow the recharge/discharge of MSE, but this effect is weakest in the austral summer season. Similarly, column-integrated radiative heating also has a similar relationship with the MSE tendency (Figure 10f), suggesting the slowing of recharge/discharge of the MSE as MJO evolves. This is consistent with earlier studies (Maloney, 2009; Kiranmayi and Maloney, 2011; Inoue and Back, 2015).

The weakened relationship of MSE anomalies with SST anomalies in the DJFM season (Figure 9d) could be explained by the dominance of the horizontal advection of moisture in the model and the counteracting role of surface evaporation anomalies engendered by the corresponding SST anomalies on MSE. From Figure 9a–c, we noted that in the austral summer season, the RSM-ROMS simulation displayed the strongest relationship of SST anomalies with corresponding anomalies of surface evaporation, precipitable water, and column-integrated radiative heating, respectively. This sets up a rather unique weaker relationship between MSE and SST anomalies at the MJO time-scale relative to other seasons (Figure 9d) as these forcing terms counteract the horizontal advection of MSE more strongly in the austral summer season. Furthermore, with relatively cooler SSTs in other parts of the year, the observed seasonal preference of the MJO for the austral summer season is well simulated in RSM-ROMS simulation.

**FIGURE 10** The lead–lag correlation between (a) precipitation and the tendency of moist static energy (MSE) anomalies at Madden–Julian Oscillation (MJO) time-scales. The regression of vertically integrated MJO anomalies of (b) divergent flux of MSE, (c) horizontal advection of MSE, (d) vertical advection of MSE, (e) enthalpy fluxes, and (f) column-integrated radiative heating on vertically integrated MJO anomalies of the tendency of MSE from the regional spectral model–regional ocean modelling system (RSM–ROMS) simulation for the four seasons of austral autumn (April–May), austral winter (June–July–August), austral spring (September–October–November), and austral summer (December–January–February–March). The horizontal long dashed lines in (a) indicate the 90% confidence interval according to the *t*-test. The negative and positive lags indicate the first variable (*P*' in [a] and the tendency of MSE' in [d–f]) are lagging and leading the second variable indicated in the panel, respectively. [Colour figure can be viewed at [wileyonlinelibrary.com](http://wileyonlinelibrary.com)]



### 4 | CONCLUSIONS

In this study, we have analysed the results of an RSM–ROMS over the WP2 region. The RSM–ROMS was integrated with 20 km grid spacing for both the atmospheric and the oceanic components of the model over a 20-year period from 1986 to 2005. It is a first-of-its-kind study over the WP2 conducted with a regionally coupled ocean–atmosphere model.

The simulation verifies reasonably with observations of precipitation and SST. The spatial gradients and the variability of the mean state of precipitation, SST, and upper-air variables are found to be reasonable in the RSM–ROMS simulation relative to observations. The

verification of the RSM–ROMS simulation highlights the simulation of the dry equatorial Pacific tongue between the ITCZ and the SPCZ. However, there is a dry bias over the SPCZ region that also stems from the near-zonal orientation of the SPCZ in RSM–ROMS as opposed to the northwest–southeast tilt in the observations. The SST simulation in RSM–ROMS produces the distinct WP2 with the cold equatorial Pacific tongue. However, the RSM–ROMS produces a warm bias over the WP2.

Despite some of these mean biases the MJO simulation in the RSM–ROMS is encouraging. The phase composite diagrams of the 20–90 days MJO anomalies largely conform to observational features relating to its eastward propagation characteristics. The MJO variability

of precipitation is, however, relatively weaker along the equatorial Pacific and north of it in the RSM-ROMS simulation compared to the observed estimates. Nonetheless, the unique observed pattern of MJOs peaking in austral winter over the WP2 region (140°E–160°E and 15°S–5°S) is nearly replicated in the RSM-ROMS simulation.

Our analysis to understand this unique pattern of MJO over the WP2 region suggests that the recharge–discharge paradigm for MJO is uniquely at play during the austral summer in the coupled model simulation, engendered by the warm SSTs and its MJO variability. In this recharge–discharge mechanism, the MSE at the MJO time-scales is built prior to the peak MJO convection and is discharged after, primarily by the horizontal advection of the MSE at the MJO time-scales in the RSM-ROMS simulation. The discharge of the MSE by horizontal advection is stemmed to some extent from column-integrated radiative heating and enthalpy fluxes at these MJO time-scales, which is supported by the associated SST anomalies. In other seasons, the relationship of MJO anomalies of surface evaporation, precipitable water, and column-integrated radiative heating with corresponding anomalies of SST are slightly weaker, which further tightens the seasonal relationship between MSE and SST in the simulation. But with relatively cooler SSTs in other parts of the year, the observed seasonal preference of the MJO for the austral summer season is well simulated in the RSM-ROMS simulation. Therefore, given these seasonal features of the MJO, the role of the co-evolution of SST and the overlying atmosphere enabled by the air–sea coupling feature of the RSM-ROMS cannot be understated.

This modelling study is one of the many recent studies that test the fidelity of the model to MJO simulation/prediction (e.g. Kim *et al.*, 2019; Richter *et al.*, 2022; Rushley *et al.*, 2022; Xiang *et al.*, 2022). In some of these studies, it was found that many current operational models underestimate the MJO propagation beyond 10 days, MJO amplitude is underestimated, and the horizontal moisture advection on MJO time-scales is underestimated owing to dry bias. Some of these biases are less pronounced in the RSM-ROMS simulation but they remain. As Kim *et al.* (2014) point out, the R2 reanalysis has several deficiencies like its wet mean bias, the intraseasonal variability of precipitation is too strong with a significantly higher power in the  $n = 1$  equatorial Rossby wave, the mixed Rossby–gravity wave, and the antisymmetric MJO compared to observations. Some of these limitations of the R2 reanalysis have an impact on the mean bias in RSM-ROMS, which is still admittedly grave and we are currently working on some sensitivity studies with model parametrizations to reduce these errors.

## ACKNOWLEDGEMENTS

We acknowledge the support from NASA grants 80NSSC19K1199 and 80NSSC22K0595.

## DATA AVAILABILITY STATEMENT

The IMERG rainfall from NASA was obtained from <https://gpm.nasa.gov/data/directory>. The OISSTv2 was obtained from <https://www.ncei.noaa.gov/products/optimum-interpolation-sst>. The ERA5 reanalysis data was from <https://www.ecmwf.int/en/forecasts/datasets/reanalysis-datasets/era5>. The data from the RSM-ROMS integration and analysis scripts necessary to generate the figures in the manuscript are available from [vmisra@fsu.edu](mailto:vmisra@fsu.edu).

## ORCID

Vasubandhu Misra  <https://orcid.org/0000-0002-1345-6280>

C. B. Jayasankar  <https://orcid.org/0000-0001-5926-6653>

## REFERENCES

- Adames, A.F. & Kim, D. (2016) The MJO as a dispersive, convectively coupled moisture wave: theory and observations. *Journal of the Atmospheric Sciences*, 73(3), 913–941. Available from: <https://doi.org/10.1175/JAS-D-15-0170.1>
- Adames, A.F. & Maloney, E.D. (2021) Moisture mode theory's contribution to advances in our understanding of the Madden-Julian oscillation and other tropical disturbances. *Current Climate Change Reports*, 7, 72–85. Available from: <https://doi.org/10.1007/s40641-021-00172-4>
- Ahn, M.S., Kim, D., Kang, D., Lee, J., Sperber, K.R., Gleckler, P.J. et al. (2020) MJO propagation across the Maritime Continent: Are CMIP6 models better than CMIP5 models? *Geophysical Research Letters*, 47(11), e2020GL087250.
- Ahn, M.S., Kim, D., Park, S. & Ham, Y.-G. (2019) Do we need to parameterize mesoscale convective organization to mitigate the MJO-mean state trade-off? *Geophysical Research Letters*, 46, 2293–2301. Available from: <https://doi.org/10.1029/2018GL080314>
- Alpert, J., Kanamitsu, M., Caplan, P., Sela, J. & White, G. (1988) Mountain induced gravity wave drag parameterization in the NMC mediumrange forecast model. In: *Conference on numerical weather prediction*, 8th edition. Baltimore, MD, pp. 726–733.
- Bellenger, H., Guilyardi, E., Leloup, J., Lengaigne, M. & Vialard, J. (2014) ENSO representation in climate models: from CMIP3 to CMIP5. *Climate Dynamics*, 42, 1999–2018.
- Bladé, I. & Hartmann, D.L. (1993) Tropical intraseasonal oscillations in a simple nonlinear model. *Journal of the Atmospheric Sciences*, 50, 2922–2939.
- Carton, J.A. & Giese, B.S. (2008) A reanalysis of ocean climate using simple ocean data assimilation (SODA). *Monthly Weather Review*, 136, 2999–3017. Available from: <https://doi.org/10.1175/2007MWR1978.1>
- Chen, B. & Mapes, B.E. (2018) Effects of a simple convective organization scheme in a two-plume GCM. *Journal of Advances in*

- Modeling Earth Systems*, 10, 867–880. Available from: <https://doi.org/10.1002/2017MS001106>
- Chen, G. & Wang, B. (2018) Effects of enhanced front Walker cell on the eastward propagation of the MJO. *Journal of Climate*, 31, 7719–7738. Available from: <https://doi.org/10.1175/JCLI-D-17-0383.1>
- Chou, M.D. & Lee, K.T. (1996) Parameterizations for the absorption of solar radiation by water vapor and ozone. *Journal of the Atmospheric Sciences*, 53, 1203–1208.
- Chou, M.D., Lee, K.T., Tsay, S.C. & Fu, Q. (1999) Parameterization for cloud longwave scattering for use in atmospheric models. *Journal of Climate*, 12(1), 159–169.
- DeMott, C.A., Benedict, J.J., Klingaman, N.P., Woolnough, S.J. & Randall, D.A. (2016) Diagnosing ocean feedbacks to the MJO: SST-modulated surface fluxes and the moist static energy budget. *Journal of Geophysical Research–Atmospheres*, 121, 8350–8373. Available from: <https://doi.org/10.1002/2016JD025098>
- Dutheil, C., Bador, M., Lengaigne, M., Lefevre, J., Jourdain, N.C., Vialard, J. et al. (2019) Impact of surface temperature biases on climate change projections of the South Pacific convergence zone. *Climate Dynamics*, 53, 3197–3219.
- Ek, M.B., Mitchell, K.E., Lin, Y., Rogers, E., Grunmann, P., Koren, V. et al. (2003) Implementation of Noah land surface model advances in the National Centers for Environmental Prediction operational mesoscale Eta model. *Journal of Geophysical Research*, 108, 8851. Available from: <https://doi.org/10.1029/2002JD003296>
- Fu, C., Diaz, H. & Fletcher, J. (1986) Characteristics of the response of sea-surface temperature in the Central Pacific associated with warm episodes of the southern oscillation. *Monthly Weather Review*, 114, 1716–1738.
- Fu, X., Wang, W., Lee, J.-Y., Wang, B., Kikuchi, K., Xu, J. et al. (2015) Distinctive roles of air-sea coupling on different MJO events: a new perspective revealed from the DYNAMO/CINDY field campaign. *Monthly Weather Review*, 143, 794–812.
- Grose, M.R., Brown, J.N., Narsey, S., Brown, J.R., Murphy, B.F., Langlais, C. et al. (2014) Assessment of the CMIP5 global climate model simulations of the western tropical Pacific climate system and comparison to CMIP3. *International Journal of Climatology*, 34, 3382–3399.
- Haertel, P.T., Kiladis, G.N., Denno, A. & Rickenbach, T.M. (2008) Vertical-mode decomposition of 2-day waves and the Madden–Julian oscillation. *Journal of the Atmospheric Sciences*, 65, 813–833. Available from: <https://doi.org/10.1175/2007JAS2314.1>
- Haidvogel, D.B., Arango, H.G., Hedstrom, K., Beckmann, A., MalanotteRizzoli, P. & Shchepetkin, A.F. (2000) Model evaluation experiments in the North Atlantic Basin: simulations in nonlinear terrain-following coordinates. *Dynamics of Atmospheres and Oceans*, 32(3), 239–281.
- Hannah, W.M. & Maloney, E.D. (2011) The role of moisture–convection feedbacks in simulating the Madden–Julian oscillation. *Journal of Climate*, 24(11), 2754–2770. Available from: <https://doi.org/10.1175/2011JCLI3803.1>
- Hendon, H.H. & Liebmann, B. (1990) The intraseasonal (30–50 day) oscillation of the Australian summer monsoon. *Journal of the Atmospheric Sciences*, 47, 2909–2924.
- Hersbach, H., Bell, W., Berrisford, P., Horanyi, A., Sabater, J.M., Nicolas, J. et al. (2020) The ERA5 global reanalysis. *Quarterly Journal of the Royal Meteorological Society*, 146(730), 1999–2049. Available from: <https://doi.org/10.1002/qj.3803>
- Ho, C.-R., Yan, X.-H. & Zheng, Q. (1995) Satellite observations of upper-layer variabilities in the western Pacific warm pool. *Bulletin of the American Meteorological Society*, 76, 669–679.
- Hong, S.Y. & Pan, H.L. (1996) Nonlocal boundary layer vertical diffusion in a medium-range forecast model. *Monthly Weather Review*, 124(10), 2322–2339. Available from: [https://doi.org/10.1175/1520-0493\(1996\)124.0.co;2](https://doi.org/10.1175/1520-0493(1996)124.0.co;2)
- Huffman, G.J., Bolvin, D.T., Nelkin, E.J. & Tan, J. (2019) Integrated multi-satellite retrievals for GPM (IMERG) technical documentation. *Nasa/Gsfc Code*, 612(47), 2019.
- Inoue, K. & Back, L.E. (2015) Column-integrated moist static energy budget analysis on various time scales during TOGA COARE. *Journal of the Atmospheric Sciences*, 72, 1856–1871.
- Johnson, R.H. (1995) Variability of clouds and precipitation during TOGA COARE. In: *Proceedings international scientific conference on the tropical ocean global atmosphere program*. Melbourne, VIC: World Meteorological Organization, pp. 552–556.
- Juang, H.H., Hong, S. & Kanamitsu, M. (1997) The NCEP regional spectral model: an update. *Bull Am Meteor Soc*, 78, 2125–2143.
- Juang, H.H. & Kanamitsu, M. (1994) The NMC nested regional spectral model. *Monthly Weather Review*, 122, 3–26.
- Kanamitsu, M., Ebuzuzaki, W., Woollen, J., Yang, S.-K., Hnilo, J., Fiorino, M. et al. (2002) NCEP-DOE AMIP-II reanalysis (R-2). *Bulletin of the American Meteorological Society*, 83, 1631–1643. Available from: [https://doi.org/10.1175/bams-83-11-1631\(2002\)0832.3.co;2](https://doi.org/10.1175/bams-83-11-1631(2002)0832.3.co;2)
- Kawamura, R. (1988) Intraseasonal variability of sea surface temperature over the tropical western Pacific. *Journal of the Meteorological Society of Japan. Ser. II*, 66, 1007–1012.
- Kemball-Cook, S. & Wang, B. (2001) Equatorial waves and air–sea interaction in the boreal summer intraseasonal oscillation. *Journal of Climate*, 14(13), 2923–2942.
- Khairoutdinov, M., DeMott, C. & Randall, D. (2008) Evaluation of the simulated interannual and subseasonal variability in an AMIP-style simulation using the CSU multiscale modeling framework. *Journal of Climate*, 21, 413–431.
- Kidwell, A., Han, L., Jo, Y.-H. & Yan, X.-H. (2017) Decadal western Pacific warm pool variability: a centroid and heat content study. *Scientific Reports*, 7(1), 13141. Available from: <https://doi.org/10.1038/s41598-017-13351>
- Kiladis, G.N., Straub, K.H. & Haertel, P.T. (2005) Zonal and vertical structure of the Madden–Julian oscillation. *Journal of the Atmospheric Sciences*, 62, 2790–2809.
- Kim, D., Lee, M.-L., Kim, D., Schubert, S.D., Waliser, D.E. & Tian, B. (2014) Representation of tropical subseasonal variability of precipitation in global reanalyses. *Climate Dynamics*, 43, 517–534.
- Kim, H., Janiga, M.A. & Pegion, K. (2019) MJO propagation processes and mean biases in the SubX and S2S reforecasts. *Journal of Geophysical Research: Atmospheres*, 124, 9314–9331. Available from: <https://doi.org/10.1029/2019JD031139>
- Kiranmayi, L. & Maloney, E.D. (2011) Intraseasonal moist static energy budget in reanalysis data. *Journal of Geophysical Research*, 116, D21117. Available from: <https://doi.org/10.1029/2011JD016031>
- Krishnamurti, T.N., Subramaniam, M., Daughenbaugh, G., Oosterhof, D. & Xue, J.H. (1992) One-month forecasts of wet and dry spells of the monsoon. *Monthly Weather Review*,

- 120, 1191–1223. Available from: [https://doi.org/10.1175/1520-0493\(1992\)120,1191:OMFOWA.2.0.CO;2](https://doi.org/10.1175/1520-0493(1992)120,1191:OMFOWA.2.0.CO;2)
- Large, W.G., McWilliams, J.C. & Doney, S.C. (1994) Oceanic vertical mixing: a review and a model with a nonlocal boundary layer parameterization. *Reviews of Geophysics*, 32(4), 363–403.
- Lau, K.-M. & Shen, S. (1988) On the dynamics of intraseasonal oscillations and ENSO. *Journal of the Atmospheric Sciences*, 45, 1781–1797. Available from: [https://doi.org/10.1175/1520-0469\(1988\)045,1781:OTDOIO.2.0.CO;2](https://doi.org/10.1175/1520-0469(1988)045,1781:OTDOIO.2.0.CO;2)
- Le, P.V.V., Guilloteau, C., Mamalakis, A. & Foufoula-Georgiou, E. (2021) Underestimated MJO variability in CMIP6 models. *Geophysical Research Letters*, 48, e2020GL092244. Available from: <https://doi.org/10.1029/2020GL092244>
- Li, H., Kanamitsu, M., Hong, S.Y., Yoshimura, K., Cayan, D.R. & Misra, V. (2014) A high-resolution ocean-atmosphere coupled downscaling of the present climate over California. *Climate Dynamics*, 42(3–4), 701–714. Available from: <https://doi.org/10.1007/s00382-013-1670-7>
- Maloney, E.D. (2009) The moist static energy budget of a composite tropical intraseasonal oscillation in a climate model. *Journal of Climate*, 22, 711–729. Available from: <https://doi.org/10.1175/2008JCLI2542.1>
- Maloney, E.D. & Hartmann, D.L. (2001) The sensitivity of intraseasonal variability in the NCAR CCM3 to changes in convective parameterization. *Journal of Climate*, 14, 2015–2034.
- Maloney, E.D., Sobel, A.H. & Hannah, W.M. (2010) Intraseasonal variability in an aquaplanet general circulation model. *Journal of Advances in Modeling Earth Systems*, 2, 1–24.
- Meinen, C.S. & McPhaden, M.J. (2000) Observations of warm water volume changes in the equatorial Pacific and their relationship to El Niño and La Niña. *Journal of Climate*, 13, 3551–3559.
- Mellor, G.L. & Yamada, T. (1982) Development of a turbulence closure model for geophysical fluid problems. *Reviews of Geophysics*, 20, 851–875. Available from: <https://doi.org/10.1029/RG020i004p00851>
- Misra, V. & Jayasankar, C.B. (2022) A high-resolution coupled ocean-atmosphere simulation of the regional climate over Central America. *Climate Dynamics*, 58, 2981–3001. Available from: <https://doi.org/10.1007/s00382-021-06083-2>
- Misra, V., Mishra, A. & Bhardwaj, A. (2018) Simulation of the intraseasonal variations of the Indian summer monsoon in a regional coupled ocean-atmosphere model. *Journal of Climate*, 31, 3167–3185.
- Miura, H., Satoh, M., Nasuno, T., Noda, A.T. & Oouchi, K. (2007) A Madden-Julian oscillation event realistically simulated by a global cloud-resolving model. *Science*, 318, 1763–1765. Available from: <https://doi.org/10.1126/science.1148443>
- Moorthi, S. & Suarez, M.J. (1992) Relaxed Arakawa-Schubert. A parameterization of moist convection for general circulation models. *Monthly Weather Review*, 120(6), 978–1002.
- Moum, J.N., Pujiana, K., Lien, R.-C. & Smyth, W.D. (2016) Ocean feedback to pulses of the Madden-Julian oscillation in the equatorial Indian Ocean. *Nature Communications*, 7, 13203. Available from: <https://doi.org/10.1038/ncomms13203>
- Nakazawa, T. (1995) Intraseasonal oscillations during the TOGA COARE IOP. *Journal of the Meteorological Society of Japan. Ser. II*, 73, 305–319.
- Pegion, K. & Kirtman, B.P. (2008) The impact of air–sea interactions on the simulation of tropical intraseasonal variability. *Journal of Climate*, 21, 6616–6635. Available from: <https://doi.org/10.1175/2008JCLI2180.1>
- Raymond, D.J. & Fuchs, Ž. (2009) Moisture modes and the Madden-Julian oscillation. *Journal of Climate*, 22(11), 3031–3046. Available from: <https://doi.org/10.1175/2008JCLI2739.1>
- Reynolds, R.W., Smith, T.M., Liu, C., Chelton, D.B., Casey, K.S. & Schlax, M.G. (2007) Daily high-resolution-blended analyses for sea surface temperature. *Journal of Climate*, 20(22), 5473–5496.
- Richter, J.H., Glanville, A.A., Edwards, J., Kauffman, B., Davis, N.A. & Jaye, A. (2022) Subseasonal Earth system prediction with CESM2. *Weather and Forecasting*, 37, 797–815. Available from: <https://doi.org/10.1175/WAF-D-21-0163.1>
- Roundy, P.E. (2012) Observed structure of convectively coupled waves as a function of equivalent depth: Kelvin waves and the Madden-Julian oscillation. *Journal of the Atmospheric Sciences*, 69, 2097–2106. Available from: <https://doi.org/10.1175/JAS-D-12-03.1>
- Rushley, S.S., Janiga, M.A., Ridout, J.A. & Reynolds, C.A. (2022) The impact of mean state moisture biases on MJO skill in the Navy ESPC. *Monthly Weather Review*, 150, 1725–1745. Available from: <https://doi.org/10.1175/MWR-D-21-0225.1>
- Shchepetkin, A.F. & McWilliams, J.C. (2005) The regional oceanic modeling system (ROMS): a split-explicit, free-surface, topography-following-coordinate oceanic model. *Ocean Modelling*, 9(4), 347–404.
- Shinoda, T., Hendon, H.H. & Glick, J. (1998) Intraseasonal variability of surface fluxes and sea surface temperature in the tropical western Pacific and Indian oceans. *Journal of Climate*, 11, 1685–1702.
- Sobel, A. & Maloney, E. (2012) An idealized semi-empirical framework for modeling the Madden-Julian oscillation. *Journal of the Atmospheric Sciences*, 69(5), 1691–1705. Available from: <https://doi.org/10.1175/JAS-D-11-0118.1>
- Sobel, A. & Maloney, E. (2013) Moisture modes and the eastward propagation of the MJO. *Journal of the Atmospheric Sciences*, 70, 187–192. Available from: <https://doi.org/10.1175/JAS-D-12-0189>
- Sobel, A., Wang, S. & Kim, D. (2014) Moist static energy budget of the MJO during DYNAMO. *Journal of the Atmospheric Sciences*, 71, 4276–4291.
- Sobel, A.H. & Gildor, H. (2003) A simple time-dependent model of SST hot spots. *Journal of Climate*, 16, 3978–3992.
- Stephens, G.L., Webster, P.J., Johnson, R.H., Engelen, R. & L’Ecuyer, T. (2004) Observational evidence for the mutual regulation of the tropical hydrological cycle and tropical sea surface temperatures. *Journal of Climate*, 17, 2213–2224. Available from: [https://doi.org/10.1175/1520-0442\(2004\)017<2213:OEFTMR>2.0.CO;2](https://doi.org/10.1175/1520-0442(2004)017<2213:OEFTMR>2.0.CO;2)
- Tiedtke, M. (1983) The sensitivity of the time-mean large-scale flow to cumulus convection in the ECMWF model. In: *Proceedings of ECMWF workshop on convective in large-scale models*. Reading: European Centre for Medium-Range Weather Forecasts, pp. 297–316.
- Umlauf, L. & Burchard, H. (2003) A generic length-scale equation for geophysical turbulence models. *Journal of Marine Research*, 61(2), 235–265.
- Wang, B. & Xie, X. (1998) Coupled modes of the warm pool climate system. Part I: the role of air–sea interaction in maintaining Madden-Julian oscillation. *Journal of Climate*, 11, 2116–2135.
- Wang, S. & Sobel, A.H. (2022) A unified moisture mode theory for the Madden-Julian oscillation and the boreal summer intraseasonal oscillation. *Journal of Climate*, 35(4), 1267–1291.

- Wang, S., Sobel, A.H., Zhang, F., Sun, Y.Q., Yue, Y. & Zhou, L. (2015) Regional simulation of the October and November MJO events observed during the CINDY/DYNAMO field campaign at gray zone resolution. *Journal of Climate*, 28, 2097–2119.
- Webster, P.J. & Lukas, R. (1992) TOGA COARE: the coupled ocean-atmosphere response experiment. *Bulletin of the American Meteorological Society*, 73, 1377–1416. Available from: [https://doi.org/10.1175/1520-0477\(1992\)073<1377:TCTCOR>2.0.CO;2](https://doi.org/10.1175/1520-0477(1992)073<1377:TCTCOR>2.0.CO;2)
- Woolnough, S.J., Slingo, J.M. & Hoskins, B.J. (2000) The relationship between convection and sea surface temperature on intraseasonal timescales. *Journal of Climate*, 13, 2086–2104. Available from: [https://doi.org/10.1175/1520-0442\(2000\)013,2086:TRBCAS.2.0.CO;2](https://doi.org/10.1175/1520-0442(2000)013,2086:TRBCAS.2.0.CO;2)
- Wu, Z. & Huang, N.E. (2009) Ensemble empirical mode decomposition: a noise-assisted data analysis method. *Advances in Adaptive Data Analysis*, 1, 1–41. Available from: <https://doi.org/10.1142/S1793536909000047>
- Wu, Z., Huang, N.E. & Chen, X. (2009) The multi-dimensional ensemble empirical mode decomposition method. *Advances in Adaptive Data Analysis*, 1, 339–372. Available from: <https://doi.org/10.1142/S1793536909000187>
- Wyrski, K. (1985) Water displacements in the Pacific and the genesis of El Niño cycles. *Journal of Geophysical Research*, 90(C4), 7129–7132.
- Xiang, B., Harris, L., Delworth, T.L., Wang, B., Chen, G. & Chen, J.-H. (2022) S2S prediction in GFDL SPEAR: MJO diversity and teleconnections. *Bulletin of the American Meteorological Society*, 22, E463–E484. Available from: <https://doi.org/10.1175/BAMS-D-21-0124.1>
- Yan, X.-H., Ho, C.-R., Zheng, Q. & Klemas, V. (1992) Temperature and size variabilities of the western Pacific warm pool. *Science*, 258(5088), 1643–1645.
- Yasunaga, K. & Mapes, B.E. (2012) Differences between more-divergent vs. more-rotational types of convectively coupled equatorial waves. Part I: space–time spectral analyses. *Journal of the Atmospheric Sciences*, 69, 3–16. Available from: <https://doi.org/10.1175/JAS-D-11-033.1>
- Zhang, C. (1996) Atmospheric intraseasonal variability at the surface in the tropical western Pacific Ocean. *Journal of the Atmospheric Sciences*, 53, 739–758.
- Zhang, C. (2005) Madden-Julian oscillation. *Reviews of Geophysics*, 43, RG2003. Available from: <https://doi.org/10.1029/2004RG000158>
- Zhao, Q. & Carr, F.H. (1997) A prognostic cloud scheme for operational NWP models. *Monthly Weather Review*, 125(8), 1931–1953.

## SUPPORTING INFORMATION

Additional supporting information can be found online in the Supporting Information section at the end of this article.

**How to cite this article:** Misra, V. & Jayasankar, C.B. (2023) Characterizing the Madden–Julian Oscillation in the western Pacific Ocean from a regional coupled ocean–atmosphere model simulation. *Quarterly Journal of the Royal Meteorological Society*, 1–17. Available from: <https://doi.org/10.1002/qj.4620>

1 **Supplementary Material**

2 **Characterizing the Madden-Julian Oscillation in the Western Pacific Ocean from a**  
3 **Regional Coupled Ocean-Atmosphere Model Simulation**

4 Vasubandhu Misra<sup>1, 2, 3, #</sup> and C. B. Jayasankar<sup>2, 3</sup>

6 <sup>1</sup>Department of Earth, Ocean and Atmospheric Science, Florida State University, Tallahassee,  
7 Florida, U. S. A.

8 <sup>2</sup>Center for Ocean-Atmospheric Prediction Studies, Florida State University, Tallahassee,  
9 Florida, U. S. A.

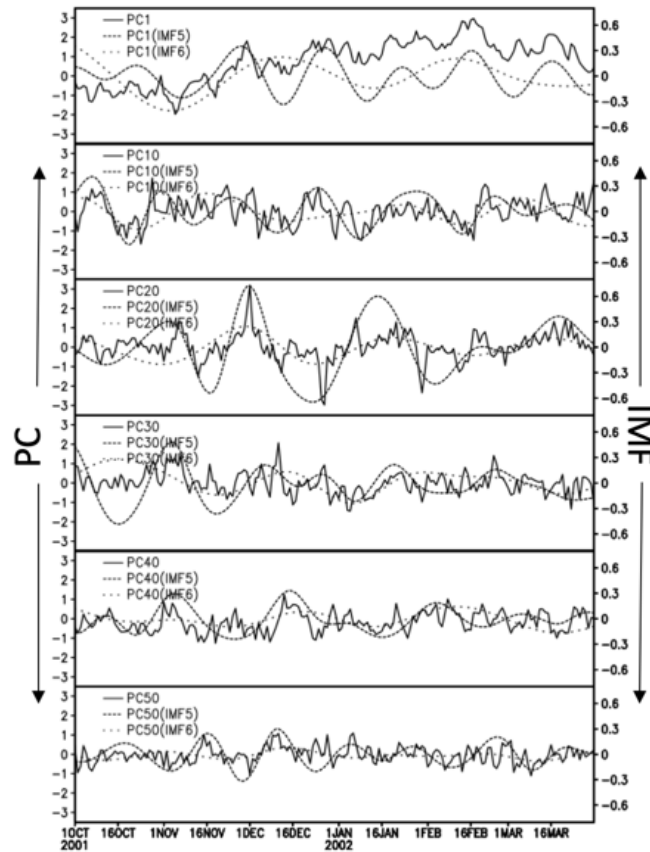
10 <sup>3</sup>Florida Climate Institute, Florida State University, Tallahassee, Florida, U. S. A.

11  
12  
13 # Corresponding Author Email: [vmisra@fsu.edu](mailto:vmisra@fsu.edu)  
14

15 **Table S1:** A brief outline of RSM-ROMS

<b>Atmospheric Model (RSM)</b>	<b>Reference</b>
28 vertical terrain following sigma levels with double sine-cosine series with wall boundary conditions as basis functions for horizontal discretization	Juang and Kanamitsu (1994)
Gravity wave drag	Alpert et al. (1988)
Longwave radiation	Chou et al. (1999)
Shortwave radiation	Chou and Lee (1996)
Land Model	Ek et al. (2003)
Boundary layer	Hong and Pan (1996)
Deep convection	Moorthi and Suarez (1992)
Clouds	Zhao and Carr (1997)
<b>Ocean Model (ROMS)</b>	
30 vertical sigma levels on horizontal staggered Arakawa-C grid	(Haidvogel et al. 2000; Shchepetkin and McWilliams 2005)
Boundary layer formulation	K-profile (Large et al. 1994)
Mixing scheme	Mellor and Yamada (1982); Umlauf and Burchard (2003)

16

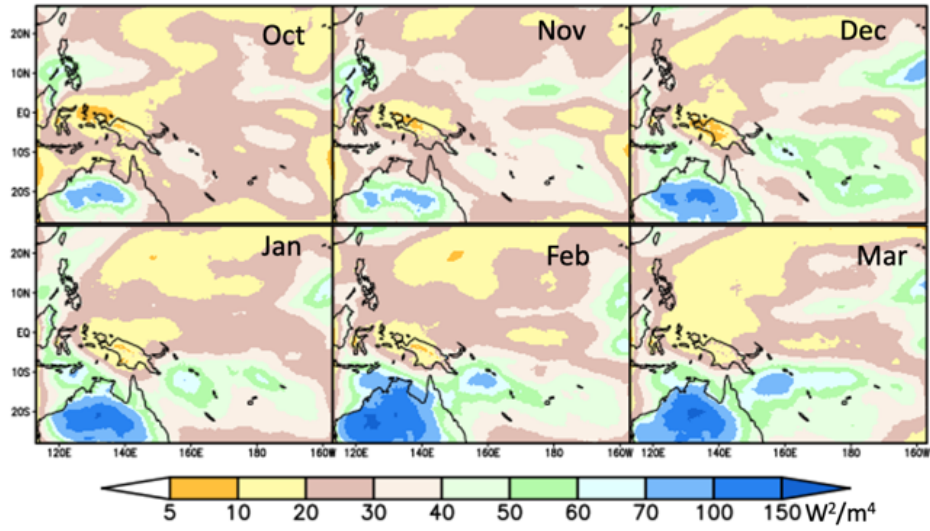


18

19 **Figure S1:** An illustration of the time series of six sample PCs (1, 20, 30, 40, and 50) amongst the  
 20 first 50 retained PCs of precipitation from the RSM-ROMS simulation and the corresponding  
 21 intraseasonal IMFs obtained by conducting EEMD. The time series is shown for the period  
 22 0000UTC 01 October 2001 to 0000UTC 31 March 2002. The ordinate on the left represents the  
 23 amplitude of the PC and the amplitude of the IMFs is shown on the right.

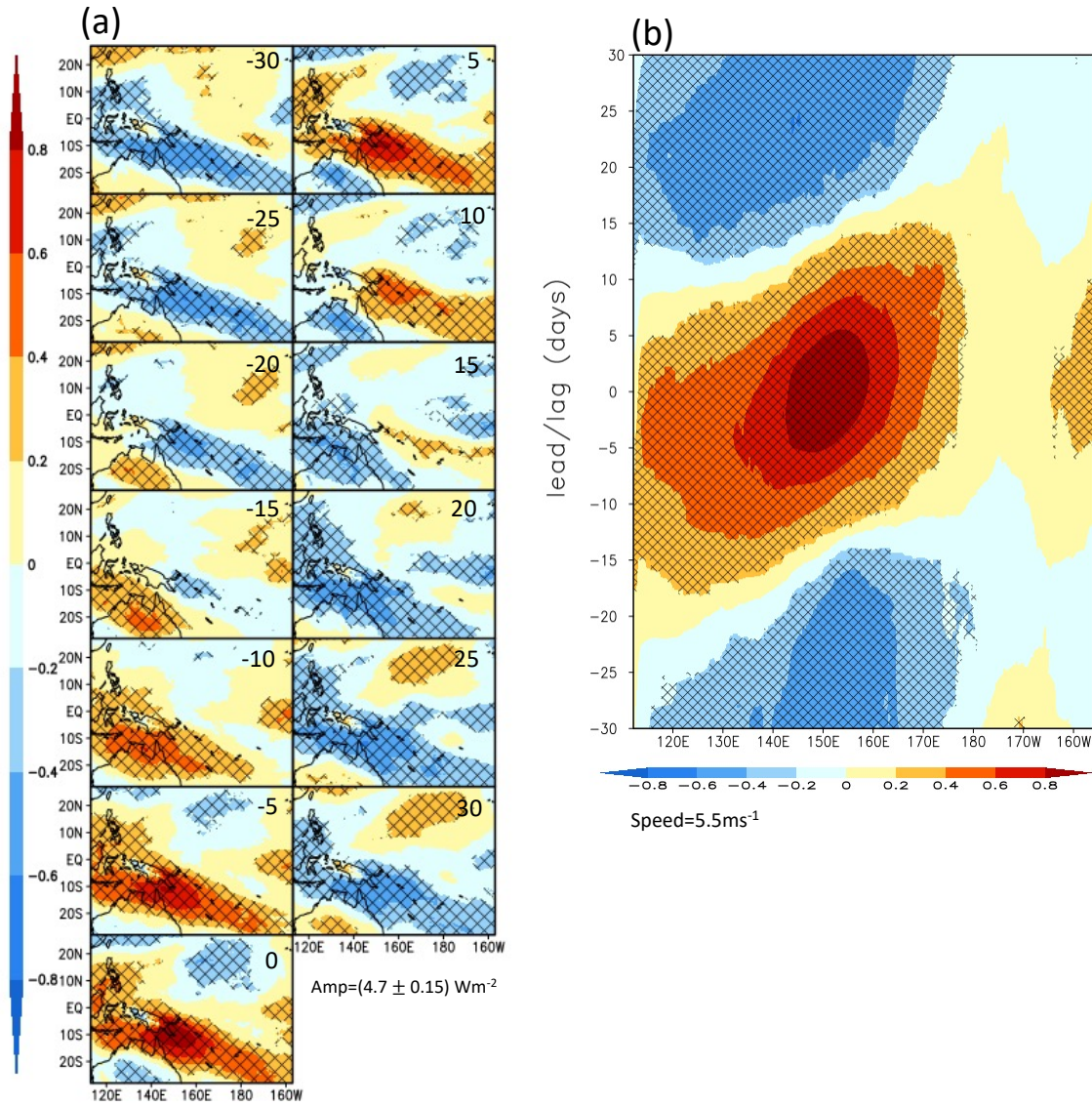
24

25

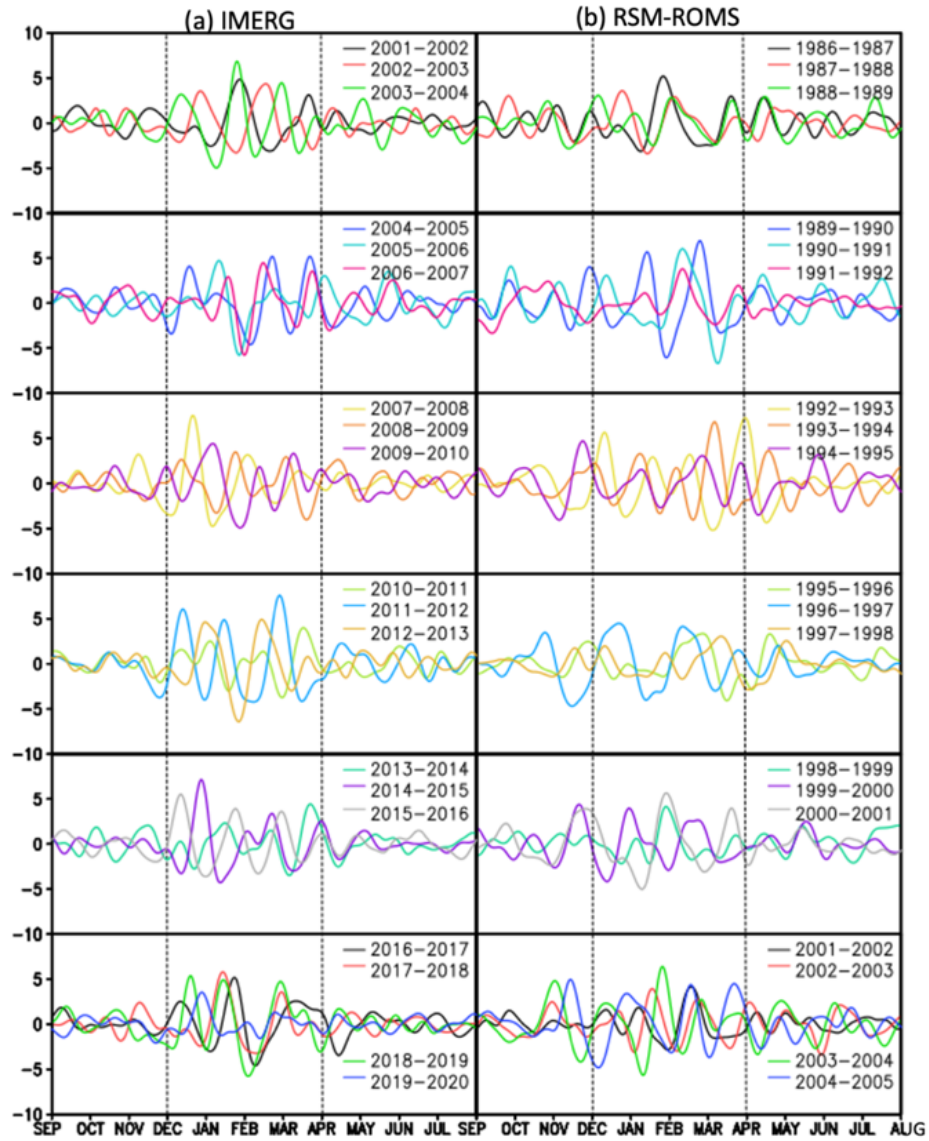


26  
27  
28  
29

**Figure S2:** The climatological monthly mean intraseasonal (20-90 days) variance of OLR anomalies from the RSM-ROMS simulation.



30  
 31 **Figure S3:** a) The regression of the intraseasonal OLR anomalies on the corresponding area  
 32 averaged intraseasonal OLR anomalies over WP2 (140°E-160°E and 15°S-5°S) from RSM-  
 33 ROMS simulation. The lead/lag in days are shown in the top right corner of each panel with  
 34 negative and positive days suggesting lead and lag with respect to the area averaged anomalies.  
 35 The hatched regions show statistically significant regions at 95% confidence interval according to  
 36 t-test. b) The regression of the intraseasonal OLR anomalies averaged between 15°S and 5°S on  
 37 the corresponding area averaged intraseasonal precipitation anomalies over WP2 from RSM-  
 38 ROMS simulation. The negative and positive days along the ordinate suggest lead and lag with  
 39 respect to the area averaged anomalies. The hatched regions show statistically significant regions  
 40 at 95% confidence interval according to t-test. The amplitude (Amp) and phase speed (Speed) of  
 41 the intraseasonal OLR anomalies over WP2 are indicated in the bottom of panels (a) and (b),  
 42 respectively.  
 43



44  
45  
46  
47  
48  
49

**Figure S4:** The annual time series of the intraseasonal (20-90 days) anomalies of precipitation (mm/day) averaged over WP2 (140°E-160°E and 15°S-5°S) from a) IMERG observations (2001-2020) and b) RSM-ROMS simulation (1986-2005).